Structural Systems and Paragenetic Assemblages at the Dominga Fe-Cu Deposit: Tectono-Metallogenic Evolution

Veloso, E.[1] (corresponding author), Email: eaveloso@gmail.com
Cembrano, J.[2], Email: jcembrano@ing.puc.cl
Arancibia, G.[2], Email: garancibia@ing.puc.cl
Heuser, G.[2], Email: gkheuser@uc.cl
Neira, S.[3], Email: sergio.neira@andesiron.cl
Siña, A.[3], Email: armando.sina@andesiron.cl
Garrido, I.[3], Email: ivan.garrido@andesiron.cl
Vermeesch, P.[4], Email: p.vermeesch@ucl.ac.uk
Selby, D. [5], Email: david.selby@durham.ac.uk
Santibáñez, I.[2], Email: ivsantibanez@uc.cl
Pérez-Flores, P.[2], Email: pvperez1@uc.cl
Gomila, R.[2], Email: ragomila@uc.cl

[1] Fundación Norte Sustentable, Avenida Cerro El Plomo 5460, Piso 19, Las Condes, Santiago, Chile.
[2] Departamento de Ingeniería Estructural y Geotécnica, Pontificia Universidad Católica de Chile, Avenida Vicuña Mackenna 4860, Macul, Santiago, Chile.
[3] Andes Iron SpA, Avenida Cerro El Plomo 5460, Piso 19, Las Condes, Santiago, Chile.
[4] Department of Earth Sciences, University College London, Gower Street, London WC1E 6BT, UK.
[5] Department of Earth Sciences, University of Durham, Durham DH1 3LE, UK.

Abstract

The Dominga district, northern Chile, shows a spatial and genetic affinity among distinctive structural elements and occurrence of Fe-Cu-rich paragenetic mineral assemblages. Deep seated, NE-to-EW striking structural elements form a right-lateral duplex-like structural system (Early Structural System, ESS) that cut regionally altered (stage I) rocks. The system served as a locus and as path for the emplacement of a Biotite-Magnetite alteration/mineralization (stage IIa) as veins and Fe-bearing layers following altered volcano-sedimentary strata. NW-striking Actinolite-Magnetite hydrothermal breccias, coeval with and part of the ESS, include Apatite (stage IIb) crystallized at ca. 127.0±15.0 Ma (U-Pb). The ESS was also the loci of a alteration/mineralization represented by K-Feldspar and Albite (stage IIIa) and Fe-Cu-rich (Vermiculite-Anhydrite-Chalcopyrite, stage IIIb) mineral associations. Shallowly developed, NNE-striking, left-lateral structural elements defining El Tofo Structural System (ETSS) – probably part of the Atacama Fault System – clearly crosscut the ESS. Minerals associated with alteration/mineralization stage IIIb also occurs as veins and as part of hydrothermal breccias of the ETSS, marking the transition from the ESS to ETSS. Molybdenite crystals associated to alteration/mineralization stage IIIb indicate an age of 127.0±0.65 Ma (Re-Os). Both the ESS and ETSS were cut by left-lateral, NW- to EW-striking shallowly developed structural elements (Intermediate Structural System, ISS) on where a Hematite-Calcite-rich paragenetic assemblage (stage IV) occurs mostly as infill material of veins and fault-veins. The ISS is, in turn, cut by NS-striking, left-lateral, shallowly developed structural elements (Late Structural System, LSS) with no evidence of alteration/mineralization. Estimated strain and stress fields indicate an overall NW-trending shortening/compression and NE-trending stretching/tension strike-slip regime, probably due to left-oblique subduction during the Mesozoic. However, the orientations of the stress and strain fields calculated for each structural system suggest a back-and-forth rotation/shift pattern – as fields change between transtensional and tranpressional – as transition between structural systems and between alteration/mineralization stages.

Keywords: Fe-rich deposit, Structural elements and systems, Stress and Strain, Mineral Paragenesis, Isotopic dating.

1. Introduction

The Dominga deposit, located ca. 60 km north of La Serena (Fig. 1), corresponds to an Fe-Cu-rich ore deposit emplaced into volcano-sedimentary rocks correlated to the Punta del Cobre Formation (e.g. Creixell y Arévalo, 2009) and into previously uncharted subvolcanic bodies of dioritic composition including andesitic and dioritic porphyries and microdiorites, altogether referred as the Porphyric Dioritic Complex. Perhaps due to its geographic location and mineralogical similarities with other Fe-rich deposits in the region, Dominga may be included within the so-called NS-striking "Cretaceous Iron Belt" (e.g. Geijer, 1931; Ruiz et al., 1965; Park, 1972; Espinoza, 1984, 1990; Oyarzún and Frutos, 1975, 1984; Menard, 1986; Ruiz and Peebles, 1988) extending from the localities of Taltal to La Serena and subparallel to the actual Coastal Cordillera in Northern Chile (Fig. 1). The belt includes several world-class IOCG (Fe-Cu-Au-Ag-U-Co-REE) deposits of Mesozoic age (e.g. Marschik et al., 1997; Marschik and Fontboté, 2001; Mathur et al., 2002; Arévalo et al., 2006; Gelcich et al., 2005; Arévalo et al. 2009;), on where mineralization occurs as veins, hydrothermal breccias and/or stratiform bodies, or, simply, as irregular-shaped bodies (e.g. Vivallo et al., 2008; Vivallo, 2009).

Several deposits within the belt are spatially and/or temporally associated with left-lateral NNE- to N-striking and NNW- to WNW-striking structural elements (e.g. Candelaria, Carola, Manto Verde and Teresa de Colmo deposits). Due to similarities in kinematics and orientation of associated structural elements, plus available geochronological data, the genesis of these deposits has been either assigned or correlated to the Atacama Fault System (AFS) (e.g. Vila et al., 1996; Sillitoe, 2003). Consistently, several models that link the activity of the AFS and different alteration/mineralization stages in Fe-rich deposits in northern Chile have been proposed (e.g. Arévalo et al. 2009; Marschik et al., 1997; Marschik and Fontboté, 2001; Mathur et al., 2002; Gelcich et al., 2005; Arévalo et al., 2006). However, certain deposits spatially within the "Cretaceous Iron Belt" are instead related to right-lateral NE- to ENE-striking structural elements apparently unrelated and previous to the activity of the AFS (e.g. Cembrano et al., 2009); as for example the deposits of Cerro Negro, El Salado (Gelcich et al., 1998), Carrizal Alto (Ruiz et al., 1965) and Mantos de Punitaqui (Ruiz et al., 1965) (Fig. 1). Some other deposits seem to be partly related to such NE- to ENE-striking structural elements; for example, at Candelaria, Bonson et al. (1998) describes a set of NE-striking right-lateral structural elements that host part of the mineralization, but assigned them to the, left-lateral, AFS.

Available geochronological data for some Fe-rich deposits spatially within the metallogenic belt argue for a main mineralization stage in the range of ca. 125-100 Ma, somehow synchronous with the left-lateral activity of the AFS (Arévalo et al., 1999; Marschik et al., 1997; Vila, 1996; Marschik and Fontboté, 2001; Ulrich and Clark, 1999; Scheuber and González, 1999; Mathur et al., 2002; Grocott and Taylor, 2002; Vivallo et al., 2008; Creixell et al., 2009; Creixell and Arévalo, 2009; and references therein). However, Fe-rich deposits associated with right-lateral structural elements seem to be somehow older (>125-140Ma; e.g. Gelcich et al., 2005), thus arguing for a possible earlier, unrelated to the AFS, mineralization stage.

This opens the possibility that alteration/mineralization associated with right-lateral NE-striking structural elements may have been overseen or wrongly assigned to the AFS on some of the Fe-rich deposits in northern Chile. If so, implies that (at least part of) the Fe-rich mineralization could be unrelated to – and older than – the activity of the AFS (e.g. Grocott and Taylor, 2002; Cembrano et al., 2009). It also implies that the traditional view of one NS-striking metallogenic belt may be biased, a misleading concept that hinders the understanding of Fe-ore formation and of mineral exploration in northern Chile. Then the question arises to whether the Dominga ore deposit was the result of a pre-, syn- or post-AFS mineralization stage? in particular, are the structural elements at Dominga associated with the AFS? or, instead, with another independent structural system?

At the Dominga district, Fe-rich mineralization occurs as veins, hydrothermal breccias and strata-like bodies, spatially and geometrically associated with particular structural elements having defined morphologies and preferential displacement and striking directions. These structural elements are: (1) NE- to EW-striking, right-lateral, foliated ultracataclasites and cataclasites, which seem to form a kilometer-size duplex geometry; (2) NNW- to EW-striking breccias bodies and other shear zones with left-lateral displacement sense; (3) NS- to NE-striking, left-lateral cataclasites, fault-breccias, slip-surfaces and fault-veins; and (4) NW- and NE-striking hydrothermal breccias. Besides differences in orientation and kinematics, structural elements show marked differences in morphology, style of deformation, average width and associated mineral assemblages (Fig. 2, 3). Then, we ask, which set or sets of structural elements host the main Fe-ore mineralization? Did these structural elements provide the necessary conditions for fluid migration and/or later emplacement? Did any or some of these sets of structural elements only modify the geometry of the ore deposit?

In this work, we present newly collected, processed and integrated structural, mineral paragenesis and isotopic data used to construct a conceptual model that accounts for the tectono-metallogenic evolution of the Dominga Fe-rich deposit. The model focuses on the spatial and temporal relations among and between structural elements, structural systems and alteration/mineralization stages. Heterogeneous, polyphasic, fault-slip data was analyzed to estimate the orientation and characteristics of the strain and stress fields that drove the tectonic evolution of the district. Paragenetic and isotopic data provide relative and absolute chronology constraints between and among alteration and mineralization mineral phases and alteration/mineralization stages.

2. Methodology

Within the Dominga district we measured a total of 962 structural elements including foliated ultracataclasites and cataclasites, non-foliated cataclasites, fault- and hydrothermal breccias, gouge bands, slip-surfaces, fault-veins and veins filled with different mineral assemblages (Fig. 2, 3). Also included, yet less exposed, are mylonites and veins showing evidence of polyphase deformation. Data logged from each structural element includes: (1) thickness, (2) orientation, (3) orientation of the slickenline (or any other kinematic indicator; e.g., Petit, 1987; Doblas, 1998), (4) the sense of displacement (e.g. Angelier, 1994; Petit, 1987), and (5) associated mineral occurrences. Among gathered data, only slip-surfaces and fault-veins (n=261) have complete fault-slip datum suitable for further strain and stress analyses (Fig. 2c).

We also recorded the orientation of foliation (S) and shear (C) planes from S-C textures macroscopically observed on foliated ultracataclasites and cataclasites (Fig. 2d) and used them to calculate the orientation of the slip direction on the C-plane. This corresponds to the vector on the C plane normal to the intersection of C and S planes. The sense of displacement was taken from the angular relationship between the same C and S planes. We considered this as a second set of fault-slip data (hereafter referred as S-C derived fault-slip data) suitable for estimation of both strain and stress fields.

Mineral occurrence – spatially and/or locally associated with an structural element – its relative concentration, grain-size, crosscutting relationships, crystal morphology, as well as the relative orientation and location with respect to nearby structural elements were logged on and locally around each structural element. We also examined under optical microscope a total of 58 thin sections (20 of them oriented), collected both from surface and from drill cores, to aid identification and definition of

mineral paragenetic assemblages, their relative temporal relationships, grain-size and morphology, and spatial and/or temporal relations with related structural elements.

Strain analysis, carried with the aid of the FaultKin software (v7.0, freely available at http://www.geo.cornell.edu/geology/faculty/RWA/programs/faultkin.html), transforms the fault-slip datum into a pair of axes representing the maximum (shortening, P) and minimum (stretching, T) strain axes (e.g. Marrett and Allmendinger, 1990). Hence, the method only transforms the fault-slip datum into a pair of orthogonal and kinematically related axes whose orientation depends on that of the structural element and of the kinematic indicator. The averaged orientations of P and T axes could then provide the overall shortening and stretching orientations at the study area or at a regional scale.

Stress analyses were conducted using the Multiple Inverse Method (MIM v4.17/6.02; Yamaji, 2000; http://www.kueps.kyoto-u.ac.jp/~web-bs/tsg/software/mim/). The method has been developed to separate homogeneous stress fields recorded on an heterogeneous fault-slip data set resulted from polyphase deformation, being successfully used to estimate and separate homogeneous stress fields from both natural and simulated heterogeneous fault-slip data sets (e.g. Sippel et al., 2009; Veloso et al., 2009; Federico et al., 2010; and references therein). The method estimates a common best-fit stress field – based on the Wallace-Bott hypothesis (Wallace, 1951; Bott; 1954) – associated with a sub-group of "k"-number fault-slip data extracted from the entire data set. The orientations of the calculated principal axes are then plotted on a couple of stereograms – one for σ_1 and other for σ_3 axes solutions (Yamaji, 2000). Each plotted axis symbol includes a tail that points towards the complementary axis (i.e. tail on σ_1 points towards σ_3), color-coded according to its stress ratio ($\phi = (\sigma_2 - \sigma_3)/(\sigma_1 - \sigma_3)$). The orientation of the best-fit stress field is then, iteratively, calculated for all possible sub-groups extracted from the entire fault-slip data set. Common and compatible stress field solutions are seen as clusters of principal axes with similar colors and with tails pointing towards a common orientation (e.g. Yamaji, 2000; Otsubo and Yamaji, 2006).

In order to estimate mineralization ages we analyzed two samples, one by means of Re-Os isotopic dating (in molybdenite) at the Sulfide and Source Rock Geochronology and Geochemistry Laboratory at Durham University, UK, and other by U-Pb isotopic dating (in apatite) at the University College of London Labs, UK. Methodology details for Re-Os dating can be obtained from Selby and Creaser (2001). In brief, molybdenite is digested in carius tube with a known about of Re and Os tracer solution with

aqua-regia. Osmium is isolated and purified via solvent extraction and micro-distillation. Re is isolated and purified by solvent extraction and anion chromatography. Both Re and Os isotope compositions were determined using Faraday cups on a Thermo Scientific TRITON mass spectrometer.

U-Pb dating was carried out by LA-ICP-MS, using a New Wave NWR 193 excimer laser with a standard volume cell connected to an Agilent 7700x quadrupole mass spectrometer. Fourteen 35μm diameter spots were ablated for 30 seconds at 10Hz and 2.5 mJ/cm^2 fluence, preceded by 15 seconds of warmup time during which blanks were collected. Madagascar (MAD) apatite was used as a U/Pb age standard (486.85 ± 0.85 Ma, Thomson et al., 2012) and NIST SRM612 as a concentration standard (Pearce et al., 1997). Sample-standard bracketing was performed using Glitter 4.4.3 (Griffin et al., 2008).

Textural and semi-quantitative chemical data were obtained through scanning electron microscopy (SEM) in a FEI Quanta 250 SEM equipped with energy-dispersive X-ray spectrometry (EDS) detector at the Department of Geology of the Universidad de Chile.

3. Structural Elements

To keep identification and classification of geological structures as simple and descriptive as possible, devoid of any *a priori* interpretation, we define a structural element as a physical planar/tabular object that may contain an infill material such as hydrothermal crystallized, magmatic, cataclastic, brecciated (sheared and broken), crystal-plastically or plastically deformed materials. Therefore, a structural element is at the outcrop scale defined by its nature and appearance, with no assumptions or interpretations involved.

Mylonites are scarce at Dominga (Fig. 2) but when present they strike ENE, ca. N60º-70ºE, yet few show NW-strikes; all with thicknesses of tens of centimeters (Fig. 3). Kinematic indicators show consistent right-lateral displacements for the NE-striking mylonites, and left-lateral for the NW-striking ones.

Foliated ultracataclasites are the most common type of structural element at Dominga, displaying a rather constant preferential ca. N60ºE-striking direction (Fig. 2). Thickness varies between few cm´s up to several tens of meters (maximum ca. 50m) (Fig. 3), yet in average they are about 10-20 cm thick. Kinematic indicators are consistent among these structural elements indicating right-lateral displacement.

Similarly, and as common as foliated ultracataclasites, foliated and non-foliated cataclasites display a NE-striking preferential orientation, yet some have N- to NNE-strikes (Fig. 2d). Thickness varies between few tens of centimeters up to ca. five meters, but in average foliated cataclasites are ca. 50 cm thick whereas non-foliated cataclasites are ca. 5-10 cm thick, slightly thicker and thinner, respectively, when compared with foliated ultracataclasites. Kinematic indicators are consistent and evidence right-lateral displacements for NE- to ENE-striking cataclasites and left-lateral displacements for those with N- to NNE-strikes.

Ultracataclasites and (foliated and non-foliated) cataclasites cut and displace the volcano-clastic rocks of the Punta del Cobre Formation, thus suggesting that these are, at least, younger than 140 Ma (e.g. Creixell and Arévalo, 2009). Included into foliated cataclasites, we found large (ca. 5-10 cm diameter) porfiroclasts of hydrothermal breccia (with a Mag-Act-rich matrix; mineral abbreviations after Whitney and Evans (2010). As shown further, hydrothermal breccia bodies also include relicts of foliated (ultra)cataclasites, similar in texture and morphology to those with preferential NE-strikes and right-lateral displacements. This suggests a coeval activity/development of the hydrothermal breccia bodies and ultracataclasites and (foliated and non-foliated) cataclasites with right-lateral displacements.

Fault-breccias display widely spread strikes with a slight preference for NE-, NNW- to NNE- and EW-strikes (Fig. 2). Thickness varies between tens of centimeters to ca. one meter (Fig. 3), being in average about 20-30 cm thick, similar to non-foliated cataclasites. No kinematic information could be obtained from these structural elements. Gouge bands, less common in the Dominga district, exhibit thicknesses ranging from few millimeters up to few centimeters (Fig. 3). Similar to fault-breccias, kinematic information from gouge bands could not be obtained with any reasonable certainty.

By definition in this work, slip-surfaces have no thickness, being essentially just striated surfaces. At Dominga, these structural elements display widespread striking directions, showing slightly preferential orientations with NW- and EW-strikes and, in a lesser amount, NNE- to ENE-strikes (Fig. 2, 3). Kinematic indicators (e.g. steps, R and R` fractures; e.g. Doblas, 1998; Petit, 1987) indicate left-lateral (with minor dip-slip, normal) displacements for NW- and for some EW-striking slip-surfaces, and right-lateral displacements for NNE- to ENE- and (some) EW-striking slip-surfaces.

Fault-veins, despite of their mineral infill, have thicknesses ranging from few millimeters up to centimeters (Fig. 3). These structural elements display clear preferential strike directions: NW, ENE and

NNE (Fig. 2, 3). Observed slickenfibers, steps and striated minerals indicate consistent left-lateral displacement with minor amounts of dip-slip (commonly normal) displacement of NE blocks.

Veins filled with different minerals (and combinations of them) outcrop all over the Dominga district (Fig. 2). Most common mineral fillings include, (either alone or associated) Mag, Ap, Qtz, Hem (specular), Act, Cal, Ep and, locally, Kfs. We also observed patches of Cu-oxides spatially associated with some minerals infills, especially those of Cal. Vein mineral filling associated with specific paragenetic associations (see further) show clear preferential strikes; for example: (1) veins with Ap or Ap+Act are common in the strike range of N30º-70ºE, whereas those with Ap+Mag tend to be more common in the strike range between N30º-50ºW; (2) veins with Hem (specular), alone or with other minerals, have strikes between ca. N10º-50ºW.

Hydrothermal breccias mostly outcrop in the easternmost part of the Dominga district. Individual bodies have tabular shapes, commonly arranged on an *en echelon* geometry (Fig 4), that can be followed tens of meters. Two distinct sets of hydrothermal breccia bodies were observed; the first in the south-easternmost part of Dominga (hereafter referred to as "Dominga Breccia") as a series of *en echelon*, subvertical bodies including massively altered clasts (Mag-Act-Ap; *ca*. 30-50%) immersed in a fine-grained matrix of Mag-Act (and Ap in places). Observed thicknesses are rather constant, being about 8-10 m. These structural elements emplaced onto altered (Fe-rich) volcano-clastic strata of the Punta del Cobre Formation, suggesting that are younger than ca. 140 Ma, as well as than the alteration/mineralization observed in the rocks of the Punta del Cobre Formation and of the Porphyric Dioritic Complex. The second set of hydrothermal breccia – outcropping in the north-easternmost part of Dominga – is a massive, irregular, and diffuse series of *en echelon*, NE-striking bodies including abundant clasts of the surrounding host rock (andesite) immersed into a matrix of massive Ap crystals. Among these elements, we found a NE-striking, tabular-shaped hydrothermal breccia subparallel to those with Ap-rich matrix, similar in texture, appearance and overall composition to the "Dominga Breccia".

Mapped and measured structural elements, regardless of its type (ultracataclasite, slip-surface, vein, etc.), can be arranged into 5 populations based on their preferential orientations. These populations of structural elements - with subvertical dips and labeled A to E on figure 2a, b – have strikes in the following ranges: (A) N50º-70ºE, (B) N30º-60ºW, (C) N80º-100ºE, (D) N20º-40ºE, and (E) Nº0-10ºE.

Population A (Fig. 2) – ca. N50º-70ºE – includes mostly ultracataclasites and (foliated and non-foliated) cataclasites showing right-lateral kinematic indicators and, to a lesser amount, by slip-surfaces

and fault-veins also evidencing right-lateral displacements. Structural elements from this population are cut and left-laterally displaced by structural elements (commonly fault-veins and slip-surfaces) with strikes between N30º-60ºW (population B; Fig. 2), suggesting that these two sets of structural elements were non-coeval.

Fe-mineralization, spatially related to the structural elements of population A, occurs as veins, massive patches and mineral clusters located either within or few meters away (<5m) from the structural elements. Also, Fe-mineralization occurs as strata-like bodies, roughly following the strata of the Punta del Cobre Formation. Thin-sections evidence that foliated ultracataclasites and (foliated and non-foliated) cataclasites contain two different types of Mag crystals with different textures, together with Act and Bt crystals which also display differences in grain-size and shape.

Population B (ca. N30º-60ºW) includes mostly slip-surfaces and fault-veins evidencing left-lateral displacements (Fig. 2a, b, 3). Ultracataclasites and (foliated and non-foliated) cataclasites are uncommon in this orientation, but when present they show left-lateral displacements (Fig. 2f). Structural elements from this population are cut, but apparently not significantly displaced, by fault-breccias, slip-surfaces and fault-veins, all with strikes between N0º-10ºE (Fig. 4). We observed slip-surfaces and fault-veins with strikes between N30º-60ºW cutting a series of tabular *en echelon* hydrothermal bodies (Mag-Act matrix) of the "Dominga Breccia".

Hem and Cal minerals (rarely together) are spatially and geometrically related to the structural elements of population B. In places, Cal-rich veins show evidences of polyphase deformation (e.g. hydrothermal or fault-breccia imposed over a former vein). Included in Cal-rich veins, we found oxidized crystals of Ccp as well as boxwork of Py/Ccp.

Population C (ca. N80º-100ºE) includes foliated ultracataclasites and cataclasites showing right-lateral displacements (S-C texture), as well as slip-surfaces and fault-veins with left-lateral kinematic indicators. Commonly, foliated ultracataclasites and cataclasites included in this population splay off similar structural elements with strikes between N50º-70ºE (population A), forming a kilometer-size right-lateral duplex geometry (Fig. 4). Similarly, slip-surfaces and fault-veins included into population C splay off similar structural elements with strikes between N30º-60ºW (i.e. population B). This later spatial arrangement is, however, fairly discontinuous – especially in the N80º-100ºE strike direction – forming a set of subsidiary structural elements rather than a duplex geometry.

Right-lateral foliated ultracataclasites and cataclasites are cut and left-laterally displaced by fault-breccias and slip-surfaces with strike directions between N30º-60ºW, but rarely by structural elements with strikes in the range N0º-10ºE (Fig. 4). Similarly, slip-surfaces and fault-veins included into population C cut and displace structural elements with strikes between N50º-70ºE (population A), as well as ultracataclasites and (foliated and non-foliated) cataclasites with strikes ranging between N80º-100ºE (population C). Thus argues for the existence of two different and independent sets of structural elements having N80º-100ºE strikes; one associated to population A and other to population B (Fig. 2a, b). Fe-bearing minerals associated with left-lateral structural elements of population C are the same as for structural elements of population B (i.e. Hem and Cal, and locally oxidized Ccp), whereas minerals associated with right-lateral structural elements of population C are the same as those of population A (i.e. Mag-Act-rich).

Structural elements defining population D (ca. N20º-40ºE) are common in the western part of Dominga, mostly outcropping nearby to an abandoned Au-Cu mine (Fig. 4). This population includes mostly foliated ultracataclasites and cataclasites, fault-breccias and slip-surfaces, which are contiguous and continuous, forming a ca. 30 meter wide composite structural element (hereafter referred as "El Tofo Deformation Band") that evidences polyphase deformation. S-C textures of foliated ultracataclasites and cataclasites within the deformation band evidence left-lateral displacement (Fig. 3c). Fault-breccias commonly contain large clasts and vein relicts with massive Mag-Act-Ap(?) crystals immersed in a cataclastic matrix (similar in texture to structural elements from population A) as well as relicts of Kfs-filled veins. Slip-surfaces and fault-veins are rarely present within the band , yet they are common few tens of meters eastward, forming an almost continuous, ca. 10m wide, band which probably represents a fault-related damage zone.

Population E consists almost solely of slip-surfaces and fault-breccias (Fig. 2) observed mostly, but not only, in the northern part of Dominga. Kinematic indicators on slip-surfaces (with strikes between N0º-10ºE) evidence left-lateral displacements. Fault-breccias commonly include relicts of crystals or veins fill with Mag-Hem, Cal or Hem.

4. Structural Systems

Structural systems refer to a series of kinematically, temporally and genetically related structural elements. Thus, different types of structural elements – such as ultracataclasites, cataclasites, fault-breccias, slip-surfaces, etc. – may be part of the same system. Differences in morphology and deformation style result from their development at different structural levels and/or under different strain/stress fields during its history (e.g. Sibson, 1987; Scholz, 2002; Passchier and Trouw, 2005).

When considering cross-cutting relationships between and among different structural elements and populations at Dominga it is possible to define four independent structural systems. Right-lateral structural elements from population A and right-lateral foliated ultracataclasites and cataclasites and fault-breccias from population C, define the oldest structural system (hereafter referred to as the Early Structural System, ESS) with an internally consistent right-lateral duplex geometry (Fig. 4). Field observations argue for a (pene)contemporaneous activity/development of these structural elements and the *en echelon* tabular-shaped hydrothermal breccias. Moreover, the geometric arrangement between these structural elements suggests that hydrothermal breccias with Mag-Act-rich matrix may have developed in a tensional orientation ("T" subsidiary structure). The ESS also includes several types of veins, mostly filled with Ap, Act, Mag, Mag+Qtz and Ep+Kfs (Fig. 2).

The structural elements of population D define a ca. N20º-40ºE striking, left-lateral structural element – hereafter termed El Tofo Structural System, ETSS – which seems to have concentrated most of the deformation without the development of other similar nearby structural elements. Structural elements from the ETSS cut and displaced those of the ESS (Fig. 4), yet they are cut and displaced by structural elements of population B and, locally, by those of population E. Only veins with Qtz+Ep fillings could be directly related to ETSS. Veins with Mag+Qtz, Mag, Ap and Ap+Act fillings (Fig. 2e) are often cut and displaced by, or included as relicts on, the structural elements of ETSS, whereas those filled with Ep+Kfs are both included as relicts and developed subparallel and within some of the structural elements of the ETSS.

Slip-surfaces and fault-veins of population B and ca. 25% of fault-veins and slip-surfaces of populations A and C, all evidencing left-lateral displacements, are geometrically related resembling a discontinuous duplex geometry. These structural elements commonly cut and displaced structural elements of the EES and the ETSS. So, similarities in morphology and kinematics plus observed crosscutting relationships suggest that (the scarce) left-lateral structural elements of population A may correspond to secondary structures of structural elements of population B, splaying off from these.

Consequently, it is possible to define an "Intermediate Structural System" (ISS) which includes the structural elements of population B and the left-lateral structural elements of populations A and C (mostly slip-surfaces, fault-veins and fault-breccias). Veins included in this system display Qtz, Qtz+Cal, Hem (specular), Cal and locally Mag and Ep (Fig. 2) as mineral infills.

Structural elements from population E mostly outcrop in the northern part of Dominga, being almost exclusively slip-surfaces and fault-breccias (Fig. 2). Observed crosscutting relationships indicate that N0º-10ºE striking structural elements cut (and displaced?) veins and fault-breccias from the ESS (Fig. 4) and fault-breccias and cataclasites of ETSS. Thus, we grouped the structural elements from population E into, and defined, a "Late Structural System" (LSS). Veins filled with Ap or with Ep and/or Ep+Qtz are commonly included as relicts within the fault-breccias of this system.

5. Strain and Stress Fields

The orientation of the strain field associated with a single structural element is uniquely defined by its principal axes (P: shortening, T: stretching; e.g. Marrett and Allmendinger, 1990). However, estimation of the best-fit strain field for a population of heterogeneous, polyphasic, fault-slip data requires filtering, sometimes subjective, of the data. Prior knowledge about the relative temporality and/or geometric relations among different structural elements may help on this (e.g. Sperner and Zweigel, 2010). Accordingly, we estimated the orientation of the strain field associated with the entire fault-slip data, each of the identified structural systems and the S-C derived fault-slip data (Fig. 5).

Estimated orientations of P and T axes from the entire fault-slip data set yielded three concentration maxima (Fig. 5a): P axes have NNW- to N- and WNW-trending azimuths with subhorizontal plunges, and T axes have NE- to E- and nearly N-trending azimuths with subhorizontal plunges. Namely, estimated strain fields correspond to strike-slip dominated deformation. However, structural elements may behave differently depending on their orientation and the chosen maxima; for example, NE-striking structural elements may behave as right- or left-lateral, depending on the maxima considered.

Strain fields estimated for each structural system yielded, in general, similar orientations of their principal axes (Fig. 5): P axes have NW- to NNW- and nearly E-trending azimuths, and T axes have NE- to ENE- and nearly N-trending azimuths, both with subhorizontal plunges. When looking at individual

solutions, we observed that the orientations of P and T axes estimated for the EES are similar to those estimated from the S-C-derived fault-slip data and roughly to one of the maxima obtained from the analysis of the entire fault-slip data (Fig. 5). Similarly, P and T axes estimated for the other structural systems have similar orientations when compared to the maximas obtained from the entire fault-slip data (Fig. 5). Despite similarities, (relative) variations on the orientation of the principal strain axes from one structural system to other are dissimilar, rotating/shifting both clock- (CW) and counterclock-wise (CCW).

Estimation of the best-fit stress field using the MIM does not need any prior assumption over the data as done previously. Clustering of principal stress axes defines a common best-fit stress tensor for a (sub)population of the fault-slip data (e.g. Yamaji, 2000; Otsubo and Yamaji, 2006; Sippel et al., 2009; Veloso et al., 2009; Federico et al., 2010). Henceforth, for the further analysis we used the entire fault-slip data without any filtering criteria yet, given the source, we considered separately the S-C-derived fault-slip data set.

Analysis of the entire fault-slip data yielded four different clusters of principal stress axes (labeled A to D on Fig. 6a). Clusters A, B and C have subhorizontally oriented principal stress axes, with trends ranging from ca. 100º to ca. 160º for the maximum (σ_1) and from ca. 20º to ca. 80º for the minimum (σ_3). Cluster D has a moderately plunging σ_1 axis (azimuth ca. 70º) and a subhorizontal σ_3 and with ca. 340º of azimuth. Thus, solutions A, B and C correspond to strike-slip regimes, whereas D is a mixture of tensional and strike-slip regimes. Stress ratio values for each solution suggest that strike-slip regimes are triaxial, varying between transpressional (TP), for solutions A and B, and transtensional (TT), for solution C. Solution D represents a stress state close to uniaxial tension.

Estimated stress fields activate particular sets of structural elements (Fig. 6). Solution A activates structural elements with strikes ranging from ca. N10ºE to N60ºW as left-lateral and those with strikes between N70º-100ºE as right-lateral. This suggests either a set of conjugate structural elements or a non-coeval activity of both sets of structural elements resulted from, roughly, similarly oriented stress fields. Solution B seems to activate structural elements with strikes slightly CW rotated/shifted with respect to those activated by solution A. However, solution B also results in normal and reverse displacements of some structural elements with strikes between ca. N30º-60ºW.

Solution C activates structural elements with strikes between N10º-30ºE as left-lateral and as right-lateral those with strikes between N70º-90ºW (Fig. 6). Solution D, on the contrary, activates structural elements with strikes between ca. N30º-70ºW as left-lateral and, to a lesser degree, those with strikes between N70º-90ºE and NW as left-lateral and as normal faulting, respectively.

Solutions E and F – obtained from the S-C-derived fault-slip data – have subhorizontal σ_1 axes with WNW- and NW-trending azimuths, respectively. The σ_3 axes of solution E are well clustered on a subhorizontal orientation, with a NE-trending azimuth; whereas solution F has rather a widespread distribution of its σ_3 axes, yet these seem to cluster close to those of solution E but with steeper plunging angles (Fig. 6). Namely, these solutions represent triaxial strike-slip and tensional/strike-slip regimes, respectively. Structural elements activated either by solutions E or F are similar, i.e. structural elements with NE- to ENE-strikes as right-lateral. Differences among structural elements activated by solution E and F are given only by a couple of fault-slip data, which may respond as left-lateral instead of right-lateral depending on which solution is considered.

6. Paragenetic Assemblages

We identified seven independent mineral associations based on contact and crosscutting relationships. Main mineral alteration phases correspond to Bt, Act, Qtz, Ep, Ab, Kfs, Anh, Allanite (Aln), Vermiculite (Vrm) and Cal; whereas mineralization mineral phases correspond to Ap, Mag, Hem (specular), Py and Ccp (Fig. 7).

The earliest identified mineral association corresponds to a mixture of disseminated, pervasively distributed, fine-grained Bt and Mag crystals spatially associated with Py and fine-grained Act, and locally with Ttn crystals (Bt≥Mag>Py>Act>Ttn association), all crystallized into the sedimentary rocks of the Punta del Cobre Formation and of the Porphyric Dioritic Complex (Fig. 7b). Mag crystals exhibit exolution textures suggesting cooling from high temperature (e.g. Butler, 1992; Tauxe, 1998).

Coarser Mag and Bt crystals display textures that coexist with Qtz, Act and Ttn, and locally, with Py crystals (Mag+Bt+Qtz±Act±Ttn>>Py association). This association occurs as disseminated or cumulated blobs of crystals (Bt+Mag-rich), as the matrix of hydrothermal breccias, as constitutive material of (ultra)cataclasites, as total or nearly complete replacement and obliteration of the host rock as

strata-like bodies, and as vein-filling material (as Bt+Qtz+Mag+Py or Qtz+Mag infills) (Fig. 7c, d). In the groundmass of andesitic rocks, part of the Porphyry Dioritic Complex, coarse-grained Mag and Bt crystals often grew onto similar fine-grained mineral phases. Mineralogically associated veins also cut rocks having disseminated fine-grained Mag, Bt and Act.

Medium- to coarse-grained Act, Ap, Qtz together with medium-grained Py and Mag crystals locally occurs as the matrix of hydrothermal breccias (Act+Mag+Py; Ap+Act+Mag+Py) and as filling material of cm-wide veins (Act+Mag+Qtz; Ap). Commonly medium-grained Mag crystals, and in places together with Py, are included in the cleavage planes of Act crystals (Fig. 7e). Field observations indicate that hydrothermal breccias with Act+Mag+Ap-rich matrix cut veins filled with and rocks altered by coarse the Mag+Bt+(Qtz±Act±Ttn)-rich association.

Veins filled with Kfs±Ep±Ab±Mag (from border to center), with Qtz+Kfs, with Qtz+Ab+Mag, and with Qtz+Ep (association Qtz>>Ep=Ab>>Kfs>>Mag) commonly cut the rocks of the Punta del Cobre Formation and of the Porphyric Dioritic Complex, as well as hydrothermal breccias with Bt+Mag+Ap matrix. Qtz-Ep-Ab association also occurs as filling material of voids in some of the volcanic rocks outcropping at the Dominga district. We also observed Kfs selectively replacing Pl crystals in andesitic rocks of the Porphyric Dioritic Complex (Fig. 7f).

Hydrothermal breccias, displaying Anh>Aln>Ccp>Py≥Mag matrix and relicts clasts with coarse-grained Bt+Mag crystals ((Anh>Aln)>Ccp>Py≥Mag association) commonly cut the massively Fe-altered strata of the Punta del Cobre Formation. Coarse-grained Bt crystals exhibit reaction borders with Ahn crystals which partially obliterate their host crystals; Aln and Ccp crystals exhibit intergrowth textures (Fig. 7g, h). Also, small veins with Ccp+Py(+Ahn?) fillings cut coarse-grained Act and Ap crystals.

Veins with a Vrm+Qtz+Py≥Ccp association infill (Fig. 7i) also cut rocks and strata strongly altered by a coarse-grained Bt+Mag-rich association. Also, medium- to coarse-grained size Mag crystals are cut by Vrm ones. Unfortunately, no other crosscutting relationships were observed, yet spatial relations among minerals phases and associations suggest that the Vrm+Qtz+Py≥Ccp paragenesis post-dates or it is penecontemponareous with the crystallization of Ep.

Hydrothermal-breccias and fault-veins exhibiting a Cal-rich matrix or slickenfibers commonly include oxidized forms and relicts of Ccp within and between Cal crystals (Fig. 7j). These hydrothermal breccias and fault-veins often cut Vrm-rich and coarse Bt+Mag-rich veins. Similarly, Qtz+Hem filled veins (Fig. 7k) commonly cut massively Mag-rich altered strata, displaying both fine- and coarse-grained

Bt+Mag crystals together with coarse Act+Mag crystals. Though rare in the field, we observe some small veins filled with Cal (center) and Hem (border).

7. Geochronological Isotopic Constraints

7.1. Re–Os dating

To provide the best age of mineralization Re-Os analysis was carried out on molybdenite (Table 1; sample DS11-134A). Although molybdenite is scarce at Dominga, trace molybdenite is observed in an Anh-matrix breccia from a drill core at 490 m depth (Fig. 8; sample DS11-134A). The breccia consists of angular clasts of host rock (Bt-altered andesite) and aggregates of Act (1.5 mm)-Bt (1 mm) into an hydrothermal matrix of coarser Ccp (up to 6 mm)-Py (8 mm) and finer Anh (1.5 mm)-All (1 mm)-Mag (0.3 mm)-Qtz (1mm). In the matrix, very fine-grained molybdenite (50-150 μm) coexists with Ahn-All-Py-Ccp-Qtz indicating that Mo and Cu mineralization occurred during the same paragenetic stage (IIIb) (Fig. 8). Cutting relationships show that Anh-matrix breccia cuts main Mag-rich ore bodies. Pure molybdenite (0.005 mg) was obtained from the sample by crushing, washing, drying, and handpicking under a microscope. The molybdenite possesses ~886 ppm Re and ~1180 ppb ^{187}Os (Table 1). The ^{187}Re-^{187}Os age of the molybdenite is 127.0 ± 0.65 Ma, which is interpreted as the time of Fe-Cu mineralization (stage IIIb).

7.2 U-Pb dating

We collected one sample containing apatite from a drill core at 170 m depth (sample DN11-136) for U-Pb dating (Table 1; sample DS11-136). Ap crystals occur mainly as the matrix of hydrothermal breccias accompanied by Mag and Act (Fig. 8). Three cm-sized fragments of apatite breccia were cut with a rock saw and polished with 4000-grit grinding paper. About 20 grains/spots were analyzed by laser ablation. Given the low (~1 ppm) U and Th concentrations and young age of the samples, common Pb is a real concern. No ^{204}Pb was measured for two reasons. First, the presence of an isobaric interference from ^{204}Hg would have compromised any ^{204}Pb correction. Second, even in the absence of ^{204}Hg, adequately measuring ^{204}Pb would require most of the analytical time at the expense of the ^{206}Pb and ^{207}Pb precision. Instead, the common Pb problem was addressed by plotting all the samples on a Wetherill concordia diagram (e.g. Ludwig, 2003), which yields a statistically robust isochron with a lower intercept of 127 Ma

± 15 Ma (95% confidence interval) and an upper intercept of meaningless age driven by the common Pb composition. It is considered the best crystallization age (500º C) of the hydrothermal apatite (Fig. 8c). Field observations suggest that Ap-rich matrix breccias are older than the Fe-Cu mineralization, which is consistent when considering the large error obtained from this sample. Additionally, no meaningful intercept at 3583 ± 110 Ma could be obtained.

8. Discussion

8.1. Structural Levels

Broadly speaking, each type of structural element outcropping at the Dominga district is related to a particular structural system. For example, nearly all structural elements of the ESS are ultracataclasites and cataclasites sharing a common preferential NE- to EW-striking orientation and right-lateral displacement direction, whereas the LSS includes mostly slip-surfaces, fault-breccias and gouge bands with a common N- to NNE-strike and with left-lateral displacements (Fig. 2). Thus, the variety of structural elements included in a particular structural system is a proxy to estimate the structural level on where they developed. In general, such depth depends on several factors (e.g. temperature, pressure, rock type, strain rate and presence of fluids; Passchier and Trouw, 2005) which also control the morphology and deformation style (e.g. Sibson, 1987; Passchier and Trouw, 2005; Holdsworth et al., 2011). Since we have no independent information about temperature, pressure or other factors, we prefer to discuss our results by referring to three general structural levels on where controlling factors are expected to be rather homogeneous: (a) deep, (2) shallow, and (3) superficial (Fig. 9). Appropriately, the brittle-plastic transition level (BPTL) divides our "deep" and "shallow" structural levels; being in general about 10 km depth, more or less independent of the rock type but strongly temperature-dependent (e.g. Sibson, 1987; Scholz, 2002; Passchier and Trouw, 2005). The BPTL may rise up to ca. 3-4 km depth if fluids (pressure) are present (Holdsworth et al., 2011). The limit between "shallow" and "superficial" structural levels is related to the depth at which deformation becomes not cohesive or discrete on a (set of) single plane (e.g. Sibson, 1987). Thus, structural elements exhibiting no mineral infill or no cohesive material (i.e. slip-surface, cracks and joints) were considered to have developed no deeper than ca. 1 km ("superficial")

depth. On the contrary, those exhibiting some infilling material (e.g. slickenfibers, matrix) were considered to have developed about 1-4 km depth ("shallow").

Accordingly, structural elements of the ESS represent the deepest (and oldest) structural system at Dominga, developed below or close to the BPTL – i.e. about 4 km depth as represented by cataclasites and ultracataclasites. The spatial relationship between these structural elements and the presence of Bt, Mag and Ap – and others –minerals suggest a direct link between the ESS and fluid mobility and arrest (e.g. Sibson, 1987; Caine et al., 1996; Cox et al. 2001) of Fe-rich fluids. Similarly, the geometric arrangement of "shallow" (slip-surfaces and fault-breccias) with respect to "deep" structural elements (ultracataclasites and cataclasites) suggest either an evolution of the system during exhumation towards shallower, more brittle, structural levels and/or a reactivation of the "deep" structural elements under a compatible younger stress field and a structural level closer to the surface.

The overall left-lateral structural elements of the ETSS – mostly fault-breccias, cataclasites and other "shallow" and "superficial" structural elements – suggests that it developed at about or above the depth of the BPTL. Here, the different structural elements most probably developed sequentially as the system accommodated to changes to the external stress field and/or to the exhumation conditions. Within the Dominga district, the general geometry of this system seems to be represented almost solely by El Tofo Deformation Band (Fig. 4) which concentrated most of the deformation. The existence of a large, and rather similar, structural element farther east (la Higuera mylonitic zone, cf. Creixell and Arévalo, 2009) argues for the occurrence of a km-size, left-lateral, duplex which may be part of the AFS (e.g. Creixell and Arévalo, 2009). However, our field data does not support the existence of a duplex arrangement between El Tofo Deformation Band and La Higuera mylonitic zone, since no kinematically (transfer) connecting structural elements were observed.

The ISS most probable developed above the BPTL, on where only exceptions are given by gouge bands (superficial), which may had developed on a later time and on a shallower structural level. Geometrically, this system seems to form a discontinuous duplex arrangement, with E-striking structural elements locally connecting NW-striking ones (Fig. 4). Interestingly, E-striking structural elements of the ISS are similarly oriented with some E-striking structural elements of the ESS, yet these show opposite displacement directions. Thus, it is possible that, at least some, E-striking structural elements developed at the time – and as part of – the ESS, were reactivated due to a different (younger) stress field as part of the ISS.

Structural elements (mostly slip-surfaces, fault-breccias, fault-veins and gouge bands) identified as part of the LSS most probably developed above the BPTL, between the depth at where the ISS developed and the surface. Structural elements of the LSS commonly cut and displace all other populations of structural elements, indicating that it is the youngest structural system outcropping in the district. Deformation is rather focused on discrete, subparallel and apparently disconnected structural elements, partially arranged on an *en echelon* geometry (Fig. 4).

Overall, it is possible to infer that exhumation at the Dominga district has been more or less steady, from the time of the ESS until the LSS. Such exhumation would be most probable no less than 3-4 km when considered the possible initial depth of the ESS.

8.2. Strain and Stress Fields

Estimated orientations of principal strain axes indicate that the different structural systems at the Dominga district are dominated by strike-slip deformation, with a general NW-shortening and a NE-stretching (Fig. 10a). However, three concentration maxima of the P and T axes (at ca. 8 and 6%; Fig. 5) were obtained from the analysis of the entire fault-slip data. The largest maxima indicates NW-shortening and NE-stretching, whereas the others indicate dissimilar orientations of the principal strain axes: N-shortening/E-stretching and WNW-shortening/NNE-stretching, respectively. These differences could be the result of the fault-slip data heterogeneity, which prevents a better resolution of the method and therefore isolation of homogeneous, independent, strain fields.

Details about the evolution of the strain field can be estimated through kinematic analyses of filtered fault-slip data (Fig. 10). The strain field associated with the ESS was estimated by using both the fault-slip data of this structural system (extracted from the entire fault-slip data set) and the S-C-derived fault-slip data (Fig. 5b, c). To estimate the strain field associated with the other structural systems (ETSS, ISS and LSS) we used the correspondent fault-slip data extracted from the entire fault-slip data set.

In general, principal strain axes are subhorizontal for each and all structural systems, thus agreeing with the previous analysis of the entire fault-slip data and supporting the idea of a strike-slip dominated deformation. Nevertheless, estimated orientations of the principal strain axes for each structural system argue for a back-and-forth rotation/shift of the strain field through time (or between structural systems).

585 Despite better estimation on the orientations of the principal strain axes from the S-C-derived
586 fault-slip data, these are fairly similarly oriented to those estimated from the ESS-filtered fault-slip data,
587 both indicating WNW-shortening (P axis) and ENE-stretching (T axis). These principal strain axes are
588 oriented between two of the maximas estimated from the analysis of the entire fault-slip data, arguing
589 against the resolution of the method to process heterogeneous, polyphasic, fault-slip data and the need of
590 fault-slip data filtering. The strain field estimated for the ESS results on right-lateral displacements of
591 NE-striking and nearly pure extension of NW-striking structural elements. These structural elements were
592 observed in the field, corresponding to ultracataclasites and cataclasites and by the Dominga breccia,
593 respectively.

594 Orientations of the principal strain axes estimated for ETSS indicate NNW-shortening and ENE-
595 stretching (Fig. 10d); which would favor left-lateral displacements on the NNE-striking El Tofo
596 Deformation band as well as on structural elements of the ESS. We did not observe left-lateral
597 displacements associated with the structural elements of the ESS, suggesting that this structural system
598 acted passively with respect to the ETSS. The strain field estimated for ETSS is rotated/shifted clockwise
599 (CW) about 40º with respect to that of the ESS; a change that most probable resulted in the abandonment
600 of the right-lateral ESS and the generation of the left-lateral ETSS.

601 For the ISS we estimated a nearly EW-shortening (P axis) and NS-stretching (T axis) (Fig. 10e)
602 strain field; that is rotated/shifted about 70º CCW with respect to that of the ETSS. The strain field
603 associated with the ISS would have favored left-lateral displacements on NW- and EW-striking structural
604 elements, and right-lateral displacements on NNE- and NE-striking ones. Field data supports left-lateral
605 displacements of NW- and EW-striking and right-lateral displacements of NE-striking structural elements
606 but no of NNE-striking ones. This suggests that the strain field associated with the ISS not only generated
607 NW- and EW-striking structural elements on a discontinuous (duplex) geometry, but also it may have
608 reactivated some of the early developed EW-striking structural elements of the ESS but with an opposite
609 sense of displacement.

610 From the ISS to the LSS, once again, the strain field rotated/shifted about 43º CW, resulting in a
611 NW-shortening axis and a NE-stretching, a strain field fairly similarly oriented to that estimated for the
612 ESS (Fig. 10). The strain field associated with the LSS would have favored: (1) left-lateral displacements
613 on NS-striking, (2) right-lateral displacements on NNE-, NE- or EW-striking, and (3) normal
614 displacements on NW-striking, structural elements. However, field data indicates left-lateral

displacements solely of NS-striking, *en echelon*, structural elements. Hence, most probably the strain field associated with the LSS did not re-activate any of the previously generated structural elements, driving only a discrete, focused, and not penetrative deformation.

Estimated stress field complement and support the deformation history depicted on the strain analysis. Given the advantages of the MIM we estimated homogeneous stress fields based on the analyses over the entire and the S-C-derived fault-slip data sets.

Stress field solutions indicate, in general, NW-compression and NE-tension (Fig. 6), a field that is quite similarly oriented when compared to the strain field estimated from the entire fault-slip data (Fig 5). In particular, we estimated four homogeneous stress field solutions that differ both in the orientation of their principal axes and in their associated stress ratios; thus, activating different sets of structural elements. Although none of the estimated solutions can be directly related to a particular structural system on a one-to-one basis (Fig. 6b), the structural elements that each solution activates can be related to particular structural systems.

Activity/generation of the structural elements of the ESS is compatible with several of the estimated homogeneous stress fields, yet all these have their principal axes fairly similarly oriented (Fig. 6, 10) suggesting a general NW-compression and an NE-tension under a strike-slip regime (e.g. Ritz, 1994). Stress ratio values vary from transtensional to transpressional: NE-striking structural elements behave mostly as transtensional, whereas those EW-striking behave as transpressional.

In time, the orientation of the stress field rotated/shifted about 15º CW, resulting in abandonment of the ESS and in generation of the ETSS. Given the composite and polyphasic architecture of El Tofo Deformation band and considering its associated stress ratio values, it is possible to argue that the band most probably developed under transtensional conditions during an early stage (perhaps inherited from the previous stress field) followed by transpressional conditions. This resulted in the development of different, independent, discrete – yet continuous and contiguous – deformation bands that concentrated most of the deformation.

Structural elements of the ISS (Fig. 4) developed during a period of general NW-compression and NNE-tension, with a significant vertical component of the maximum principal stress axis (Fig. 10) – given by the contribution of solution D. The orientation of this stress field is about 25º CCW rotated/shifted and 30º-40º tilted with respect to the orientation of the stress field estimated for ETSS. Although the structural elements of the ISS were the result of the new (at the time) stress field, some EW-

striking structural elements of the ESS may have been reactivated as left-lateral fault-breccias and fault-veins, opposite to right-lateral (ultra)cataclasites of the ESS. Stress ratio values associated with the ISS indicate a transpressional-transtensional behavior of the system. Here, NW- to NNW-striking structural elements are related to transtensional stress ratio values, whereas those striking NW to EW are mostly related to transpressional ones.

The orientation of the stress field associated with the structural elements of the LSS indicates strike-slip regime with a NW-compression and a NE-tension. The orientation of this stress field is rotated/shifted about 10º CW with respect to that estimated for the, previous, ISS. Stress ratio values for the LSS are mostly transpressional, yet some few structural elements may have behaved as transtensional.

Overall, estimated strain and stress fields indicate a general NW-SE trending shortening/compression and a NE-SW trending stretching/tension (Fig. 5, 6, 10) that experienced slight changes in orientation and between transtensional and transpressional characteristics. Principal axes of strain and stress fields estimated for each structural system are not coaxial, supporting the idea of an overall strike-slip regime, simple-shear dominated deformation during the activity of all identified structural systems. Differences in the orientation of both strain and stress fields among structural systems also argue for a back-and-forth rotation/shift through time; CW rotations are associated with transpressional conditions whereas CCW are with transtensional ones (Fig. 10c). In all cases, it seems that rotation/shift of the strain/stress field resulted in the abandonment of a particular structural system and the development of a new, independent, one.

Rotation of tectonic blocks has been proposed for the northern part of the El Salado segment of the AFS (e.g. Taylor et al., 1998; Forsythe and Chisholm, 1994; Rojas et al., 1994; Beck, 1998), which may be related to rotations/shifts of the orientations of the strain/stress fields estimated at the Dominga district. Although not reported as a rotation/shift of tectonic blocks or of strain/stress fields, Scheuber and González (1999), argue for relaxation of the overriding (South American) plate – between ca. 155 and ca. 140 Ma – during a period of overall SE-trending subduction, prior to the initiation of the AFS (e.g. Coira et al., 1982; Scheuber and Gonzalez, 1999; Grocott and Taylor, 2002). Accordingly, this would have triggered the development of right-lateral NE-striking structural elements. Given the probable pre-AFS age and the similarities in orientation between the structural elements of the ESS and those proposed by Scheuber and Gonzalez (1999), it is most probable that these correlate. This idea is supported by available geochronological constraints. The activity of the ESS is constrained by the rocks of the Punta del Cobre

675 Formation (>140 Ma; Creixell and Arévalo, 2009), by our ca. 127 Ma (U-Pb) age obtained from Ap
676 crystals as well as by the proposed age for the initiation activity of the AFS at ca. 125 Ma (Scheuber and
677 González, 1999; Grocott and Taylor, 2002). However, and given the nearly 127 Ma Re-Os age obtained
678 from Molybdenite crystals, it is most probable that the ESS ended its activity before or close to ca. 127
679 Ma (Fig. 11).

680 From the ESS to the ETSS, estimated strain/stress fields rotated/shifted CW about 40º and 15º,
681 respectively (Fig. 10). Such rotation/shift could resulted from either rotation of discrete (fault-bounded)
682 tectonics blocks – and therefore of the strain/stress fields that they recorded – or a simple rotation/shift of
683 the overall stress/strain field most probable controlled by the convergence direction of the subducting
684 plate (e.g. Scheuber and González, 1999; Grocott and Taylor, 2002). If rotation of tectonic blocks –
685 between the major lineaments of El Tofo deformation band and La Higuera Mylonitic Zone (e.g. Creixell
686 and Arévalo, 2009) – is the cause, then the ESS would have experienced a CCW rotation of, at least, 15º.
687 If so, then the ESS would had a general strike of N70º-90ºE before the development of the ETSS. Based
688 on paleomagnetic analyses in the northern part of the El Salado segment of the AFS, Taylor et al. (1998)
689 proposed a ca. 10º rotation of the Mesozoic arc at ca. 132-125 Ma, an age within that estimated for the
690 activity of the ESS (Fig. 11). On the contrary, if rotation/shift of the strain and stress fields resulted from
691 a rotation/shift of the overall subduction convergence, then the ESS would have acted as a passive
692 element, ergo being only left-laterally disrupted and displaced by the ETSS.

693 The overall N20º-40ºE trend of the ETSS is roughly subparalell to that of the AFS (e.g. Brown et
694 al, 1993) and both show similar displacement (left-lateral) direction, suggesting a spatial and temporal
695 affinity (e.g. Coira et al., 1982; Scheuber and Gonzalez, 1999; Grocott and Taylor, 2002). Hence, it is
696 highly possible that the ETSS is part (local) of the AFS, perhaps representing a splayed off arm of it. This
697 implies that the time of activity of the ETSS and the AFS can be correlated, constraining the activity of
698 the ETSS between ca. 125 to ca. 90 Ma (Scheuber and González, 1999; Grocott and Taylor, 2002).

699 Once more, we estimated a CCW rotation/shift of the strain/stress fields from the ETSS to the ISS,
700 which could have resulted from rotation of discrete tectonic blocks or from shift/rotation on the
701 convergent direction of the subducting plate. CCW rotation of tectonic blocks or of structural elements of
702 the AFS has not been reported, to the best of our knowledge, for any of its segments. Thus, the estimated
703 ca. 71º and 25º CCW rotation/shift of the strain and stress fields, respectively, estimated for the change
704 from the ETSS to the ISS structural systems is most probably related to a shift in the convergence

direction of the subducting plate. We agree with the general view that these NW-striking structural elements (ISS) are the result of a change in the general tectonic configuration of the South American Arc (e.g. Mpodozis and Ramos, 1990; Taylor et al., 1998) rather than to (a local) rotation of tectonic blocks. The shift from ETSS to the ISS most probably occurred after the cease of the activity of the AFS (ca. 90 Ma) and lasted until reconfiguration ended, i.e. ca. 80 Ma (Fig. 11) (e.g. Mpodosiz and Ramos, 1990; Grocott and Taylor, 2002).

A further CW rotation/shift of 43º and of 10º CW of the strain and stress fields, respectively, occurred between the development of the ISS and of the LSS (Fig. 10). Since structural elements of the ISS are cut and displaced by those of the LSS, the rotation/shift most probably occurred after the cease of the ISS. Unfortunately, no geochronological constraints are available, yet reported Cenozoic CW rotations in the forearc (e.g. Arriagada et al., 2006; Roperch et al., 2006; Taylor et al., 2007) could be related to the activity of the LSS. In such case, the LSS developed sometime after 80-40 Ma.

8.3. Alteration/Mineralization Stages

Identified mineral paragenetic assemblages depict the arrest of fluids and argue for a discrete evolution towards lower temperature mineral phases. The four alteration/mineralization stages defined here (labeled stages I to IV on Fig. 7) roughly correlate with similar stages defined and identified on several Fe-rich deposits in northern Chile (e.g. Arévalo et al., 2006; Marschik and Fontboté, 2001; Benavides, 2007).

Alteration/mineralization stage I – marked by the occurrence of fine-grained Bt and Mag crystals together with Act, Py and rare Ttn – is similar to alteration/mineralization mineral assemblages described, for example, in Candelaria (e.g. Arévalo, 2006), El Romeral (Bookstorm, 1977), Mantoverde (Benavides, 2007) and for the Candelaria-Punta del Cobre district in general (Marschik and Fontboté, 2001). At a regional scale, this alteration/mineralization has been interpreted as a result of a widespread metasomatism due to the emplacement of plutonic bodies during the Late Jurassic-Early Cretaceous (e.g. Arévalo, 2006; Bookstorm, 1977; Taylor et al., 1998; Marschik and Fontboté, 2001; Benavides et al., 2007; Fig. 11).

The occurrence of coarse- to medium-grained Mag, Bt and, locally, Act and Py crystals as: matrix of hydrothermal breccias, constituent material of (foliated) ultracataclasites and cataclasites, vein filling

material together with Qtz crystals, and as strata-like Fe-rich bodies that follow the strata of the rocks of the Punta del Cobre Formation, marks the beginning of alteration/mineralization stage II (Fig. 7) which corresponds to the main Fe-mineralization at Dominga. Ap crystals seem to have crystalized at a medium to later time within stage II, as evidence by crosscutting relations between veins filled with Ap, Ap+Mag and hydrothermal breccias with an Act-Ap-rich matrix. Accordingly, we prefer to divide our stage II into sub-stages IIa and IIb, defined by the lack and occurrence of Ap crystals, respectively (Fig. 7, 11). Similar paragenetic assemblages have been described for other Fe-rich deposits in the region, including Candelaria (Marschik and Fontboté, 2001), Cerro Negro (Vivallo et al., 1995), El Romeral-Algarrobo (Bookstrom, 1977; Nyström and Henríquez, 1994), Fresia and Carmen (Bonson, 1996), Productora (Ray and Dick, 2002) and Panulcillo (Correa, 2000). For example, at Candelaria, this paragenetic assemblage has been defined as "Iron Oxide Stage", representing part of the ore mineralization and partly hosted on NE-striking structural elements (Marschik and Fontboté, 2001; Arévalo et al., 2006).

Alteration/mineralization stage III (defined by the occurrence of Kfs, Ep and coarse-to medium-grained Mag crystals) was mostly observed as filling material of veins subparallel to (foliated) ultracataclasites and cataclasites, and to veins filled with Mag and Mag-Act. Crosscutting relations suggests a later growth of Anh-Aln-Vrm crystals, most probably coeval or pene-contemporaneous with Ccp-Py-Mo crystallization. Hence, we prefer to divide our alteration/mineralization stage III into sub-stages IIIa and IIIb, defined by the occurrences of Kfs±Ep and Anh-Aln-Vrm-Ccp-Py-Mo, respectively. Structural elements displaying an Anh-Aln-Vrm-related paragenetic assemblage are both subparallel to the structural elements of the ESS and of the ETSS. Moreover, relicts of Kfs filled veins are included into some fault-breccias of the El Tofo Deformation band. Crosscutting relations between Kfs-Ep and Anh-Aln-Vrm paragenetic assemblages are in places opposite, yet both are post-Act crystals (stage IIa), and pre-Hem and/or Cal-rich (stage IV) mineral assemblages. This suggests that stage III occurred between the transition from the ESS to the ETSS, probably related to the transtensional activity of both systems.

Cu-related mineralization in Fe-rich deposits in northern Chile corresponds mostly to the occurrence of Ccp, and described as accompanied by Aln and light REE in the deposits of Productora and Santa Inés (Ray and Dick, 2002). At Productora, Osterman (1997), argues for a Ccp mineralization stage, coeval (or at least pene-contemporaneous) with the occurrence of Kfs and Ep crystals. Also, for the deposit of El Romeral, Bookstrom (1977) associated a Py-Ccp-Ep paragenetic assemblage to the observed Cu-mineralization; whereas at Candelaria, Marschik and Fontboté (2001) and Marschik et al. (2000),

765 argue that the main Cu-mineralization is associated with the occurrence of Aln and Anh crystals that grew
766 after the main Fe-mineralization stage, i.e during the activity of the AFS.

767 Alteration/mineralization stage IV (Hem, Py, Ccp, oxidized Ccp and Cal; Fig. 7, 11) mostly occurs
768 as filling material of veins and as part of the matrix of hydrothermal- and fault-breccias. A similar
769 paragenetic association has been described for the deposits of Teresa de Colmo (Bonson, 1996) and
770 Candelaria (Ruiz et al., 1965; Marschik and Fontboté, 2001), and interpreted as the end of the hypogene
771 mineralization. However, the presence of oxidized forms of Ccp and the presence of Hem (specularite)
772 suggest at least a slight degree of supergene alteration.

773 The paragenetic assemblages identified at Dominga argue for a decreasing temperature of the
774 mineralizing fluids, evidenced by the change from Mag-Act-Bt-rich towards Hem-Ep-Cal-rich
775 assemblages (Fig. 7). Previously published geochemical analyses carried on mineralogically similar Fe-
776 rich deposits in the region also argue for a decreasing temperature of the mineralizing fluids, from at least
777 600º-500ºC (stage I and II) to 470º-340ºC (stage III) and down to ca. 230ºC (stage IV) (Marschik and
778 Fontboté, 2001).

779 Alteration/mineralization stages similar to those defined here have been dated using several
780 methods and materials, giving ages between 131,0±0,1 Ma (at Carmen Sur; Gelcich et al., 2005) and ca.
781 111,0 Ma (at Candelaria; Arévalo et al., 2006) (Fig. 11). At Dominga, paragenetic assemblage stage I
782 grew onto the rocks of the Punta del Cobre Formation and of the Porphyric Dioritic Complex, which are
783 no younger than 140-139 Ma (Creixell and Arévalo, 2009) (Fig. 11). This constraints the probable
784 beginning of stage I, yet it could have started as early as ca. 149 Ma when considering Ar-Ar (Act)
785 geochronological data from the Cordón de Véliz area (Fig. 11) (Vivallo et al., 2008). The end of stage I is
786 here constrained by the activity of the ESS, since its structural elements show relicts of this paragenetic
787 assemblage.

788 Although no direct constraints for the beginning of stage IIa are available, it can be argued that it
789 started after stage I, i.e. ca. 140-139 Ma, which correlates with the end of the relaxation of the upper plate
790 proposed by Scheuber and González (1999). Despite this, the occurrence of Ap crystals (stage IIb) can be
791 correlated with similar mineral occurrences at Carmen Sur, dated ca. 131 Ma (U-Pb, Ap) (Gelcich et al.,
792 2005), as well as by our ca. 127 Ma U-Pb (Ap) age (Fig. 11).

793 Age constraints for stage III are given by our U-Pb (Ap) and Re-Os (Molybdenite)
794 geochronological data, and by similar Re-Os dating at Candelaria (Mathur et al., 2002) (Fig. 11). Stage

IIIa must have started at ca. 127 Ma, slightly after or shortly overlapped with Ap crystallization. Stage IIIb started just after ca. 127 Ma, lasting until ca. 114 Ma, assuming that the occurrences of Molybdenite at Dominga and at Candelaria deposits resulted from correlated alteration/mineralization processes (Fig. 11).

Alteration/mineralization stage IV is unrelated to the ETSS (and therefore to the activity of the AFS) but to the ISS. As argued before, the ISS started after the cease of the AFS, i.e after ca. 90 Ma (i.e. Scheuber and González, 1999; Grocott and Taylor, 2002), and lasted until reconfiguration of the South American Arc ended at ca. 80 Ma (e.g. Mpodozis and Ramos, 1990; Taylor et al., 1998). Stage IV then would have lasted at most for about 10 m.y., from ca. 90 to ca. 80 Ma (Fig. 11).

8.4. Tectono-Metallogenic Evolution

As shown, alteration/mineralization stage I corresponds to a widespread, regional, metasomatic event, hence, unrelated to any identified structural system at Dominga or elsewhere among Fe-rich deposits in the region. On the contrary, the spatial orientation and locale of Mag-rich, Ap-rich and Mag-Act-rich veins and strata-like bodies, together with similar mineral contents in the matrix of ultracataclasites and cataclasites and hydrothermal breccias indicate a direct link between the ESS and stage II (Fig. 11, 12). Hence, we can argue that the emplacement of the main Fe-rich mineralization at Dominga was controlled by and occurred during the transtensional activity of the ESS.

The occurrence of veins filled with Ep and Kfs subparalell to the structural elements of the ESS, as well as the presence of Ep as constituent of the matrix of hydrothermal breccias suggest that stage IIIa occurred during the (waning?) activity of the ESS. The occurrence of Ep-related paragenetic mineral assemblages (such as Vrm-Aln-Anh) as part of the matrix of hydrothermal breccias of some of the structural elements of El Tofo Deformation Band as well as filling material of veins subparallel to the structural elements of the ESS and of the ETSS suggest that stage IIIb was contemporaneous with the both structural systems, possibly marking a transition stage between them. This argues that the main Fe-Cu-mineralization stage (III) is most probably associated with the transtensional activity of the ESS and with the earliest – most probable also transtensional – activity of ETSS. This later process of alteration/mineralization (stage IIIb) seems to correlate with various Cu-mineralizations identified on

other Fe-Cu-rich deposits in the region (e.g. Arévalo et al., 2006; Mathur et al., 2002; Marschik and Fontboté, 2001; Arévalo et al., 1999).

A late Fe-Cu-rich mineralization, represented by the mineral assemblages of stage IV, was emplaced during the activity of the ISS, after the cease of ETSS and, regionally, of the NS- to NNE-striking AFS (e.g. Grocott and Taylor, 2002; Taylor et al., 1998). This is supported by the conspicuous occurrence of Hem and Cal, both accompanied by Ccp, as mineral infill in veins, hydrothermal breccias and composite structural elements with strikes of about N30º-60ºW (Fig. 2, 12).

Field-based observations indicate that the structural elements of the LSS are unrelated to any alteration/mineralization observed at Dominga. No veins of specific alteration/mineral assemblages were found either subparallel or included into these structural elements. This activity of this system thence only modified the overall geometry of the deposit, via left-lateral, strike-slip deformation (Fig. 4, 12).

9. Conclusions

The occurrence of a Fe-Cu-mineralization at Dominga is spatially, genetically and tectonically associated with four different and independent structural systems. Strain and stress analyses performed over fault-slip data from a variety of structural elements indicate a rotation/shift of these fields during the deformation history of the Dominga deposit. The emplacement and arrest of Fe-Cu-rich fluids and the generation of the Dominga Fe-rich deposit pre-, syn- and post-dates the activity of the AFS (Fig. 11, 12). Our results can be summarized as follow:

- There is a background, regional, alteration/mineralization represented by disseminated, yet pervasive, occurrence of fine-grained Bt-Mag (-Py-Act-Ttn) crystals (stage I) in the rocks of the Punta del Cobre Formation and in the Porphyric Dioritic Complex.
- The ESS corresponds to a right-lateral duplex arrangement of deep seated (3-4 km depth) structural elements with preferential strikes between N50º-70ºE and N80º-100ºE. The main activity of this system was between ca. 139 and ca. 125 Ma, with a general transtensive regime, which controlled the mobility and arrest of Fe-rich alteration/mineralization fluids.
- The main Fe-rich mineralization/alteration at the Dominga deposit corresponds to the occurrence of coarse- to medium-grained Mag-Bt-Act-Ap paragenetic assemblage (stage II), spatially associated

with the strata of the Punta del Cobre Formation, with the Porphyric Dioritic Complex and with structural elements of the ESS such as foliated ultracataclasites and foliated and non-foliated cataclasites, veins and hydrothermal breccias. Geochronological data (Ap, U-Pb) indicates an age of ca. 127.0±15.0 Ma for the Ap crystallization (stage IIb).

- A second mineralization/alteration, related to the ESS, corresponds to the occurrence of Kfs and Ep-rich (stage IIIa) whereas a later Anh-Aln-Vrm-Ccp-rich (IIIb) alteration/mineralization is related to both the ESS and the ETSS. These two stages (IIIa and IIb) represent a second Fe-Cu-rich alteration/mineralization at the Dominga district. Geochronological data (Molybdenite, Re-Os) indicates an age of ca. 127.0±0.65 Ma for alteration/mineralization stage IIIb). The $^{206}Pb/^{238}U$ age in apatite of 127±15 Ma is considered the best estimation to the hydrothermal apatite breccia, and most probably older than the molybdenite age.
- A CW rotation/shift of both strain and stress fields caused the abandonment of the structural elements of the ESS and the development of those of the ETSS (which correlates with the AFS). The ETSS developed under trantensional/tranpressional tectonic conditions, at a depth of about the BPTL (i.e. 3-4 km) and above. Deformation was concentrated onto a composite structural element with a nearly N20º-40ºE strike preferential direction. Correlation with available geochronological data suggests that this system was active between ca. 125 and ca. 90 Ma.
- The ETSS, during an initial transtensive phase, most probably controlled the ascent and emplacement of Fe-Cu-rich fluids (stage IIIb). However, a change towards a transpressive tectonic phase resulted in the cease of alteration/mineralization stage IIIb at Dominga. The tectonic activity of ETSS also changed the initial geometry of the deposit by left-lateral disruption (and perhaps some minor rotation) of, fault-bounded, tectonic blocks.
- A CCW rotation/shift of the strain and stress fields, resulted from the change of the convergence subduction direction, caused the cease of tectonic activity on ETSS and the development of an arrangement of a series of N30º-60ºW and N80º-100ºE striking structural elements that define the ISS. This later system developed (between 90 and 80 Ma) at a shallower depth with respect to the structural elements of the ESS, yet it probably was similar to the depth at which the ETSS developed.
- The transtensional activity of the ISS was accompanied by a late Fe-Cu-rich mineralization (stage IV), represented by the occurrence of Hem and Cal (together with oxidized Ccp). Similar to the role played

by ETSS, the ISS controlled the emplacement of a late alteration/mineralization, yet it also changed the geometry of the deposit via left-lateral disruption of fault-bounded tectonic blocks.

- Finally, a CW rotation/shift of the strain and stress fields resulted in the abandonment of the ISS and the development of the LSS. The structural elements of this later system most probably developed at a shallow to superficial depth and were were, in any case, active post any identified alteration/mineralization at Dominga, thus being probably Cenozoic in age and unrelated to the main tectono-metallogenic evolution of the Dominga deposit. Thence, the LSS only modified the, already disrupted, geometry of the deposit.

Acknowledgements

We would like to thank all personnel at Dominga site for their valuable help during field campaigns. Special thanks to M. Vivanco, for his comments and suggestions in the field that helped to unravel the complex tectono-metallogenic processes at Dominga. This work was supported by a joint project venture between Andes Iron SpA and the Direction of Research and Science (DICTUC) of the Pontifical Catholic University of Chile and it is a contribution to Millennium Science Initiative NC130065.

901 REFERENCES

902

903 Angelier, J (1994) Fault slip analysis and paleostress reconstruction. In: Hancock, P. (ed.) Continental
904 Deformation. Pergamon press, UK, pp 53-100.

905 Arévalo, C (1999) The coastal Cordillera-Precordillera boundary in the Copiapó area, northern Chile and
906 the structural setting of the Candelaria Cu-Au ore deposit. Ph.D. dissertation, Kingston University

907 Arévalo, C, Grocott, J, Martin, W, Pringle, M, Taylor, G (2006) Structural Setting of the Candelaria Fe
908 Oxide Cu-Au Deposit, Chilean Andes (27°30`S). Economic Geology 101: 819-841.

909 Arriagada, C, Roperch, P, Mpodozis, C, Fernandez, R (2006) Paleomagnetism and tectonics of the
910 southern Atacama Desert (25-28 degrees S), northern Chile. Tectonics 25(4): TC4001.

911 Beck, M (1998) On the mechanism of crustal block rotation in the central Andes. Tectonophysics 299:
912 75-92

913 Benavides, J, Kyser, T, Clark, A, Oates, C, Zamora, R, Tarnovschi, R, Castillo, B (2007) The Mantoverde
914 Iron Oxide-Copper-Gold District, III Región, Chile: The Role of Regionally Derived, Nonmagmatic
915 Fluids in Chalcopyrite Mineralization. Economic Geology 102: 415–440.

916 Bonson, C. Grocott, J, Rankin, A, (1996) A structural model for the development of Fe-Cu mineralisation
917 within the Atacama Fault System, (25°00`S-27°15`S), Northern Chile. Third ISAG, St. Malo, France:
918 671-674.

919 Bookstrom, A (1977) The magnetite deposits of El Romeral, Chile. Economic Geology 72: 1101–1130.

920 Bott, M (1959) The mechanisms of oblique slip faulting. Geological Magazine 96: 109-117.

921 Brown, M, Diaz, F, Grocott, J (1993). Displacement history of the Atacama Fault System 25°-27°S,
922 northern Chile. Geological Society of America Bulletin 105: 1165-1174.

923 Butler, R (1992). Paleomagnetism: Magnetic domains to geologic terranes, Blackwell Scientific
924 Publications, Boston..

925 Caine, J, Evans, J, Forster, C (1996) Fault zone architecture and permeability structure. Geology 24:
926 1125–1128.

927 Cembrano, J, Garrido, I, Marquardt, M (2009) Tectonic setting of IOCG deposits in the Central Andes:
928 Strike-slip-dominated deformation. XII Congreso Geológico Chileno, Santiago: S9_043

929 Coira B, Davidson J, Mpodozis C, Ramos V (1982) Tectonic and magmatic evolution of the Andes of
930 Northern Argentina and Chile. Earth Science Reviews 18: 303–332.

931 Correa, A (2000) Geología del Yacimiento Fe-Cu Teresa del Colmo, Región de Antofagasta, Chile. 9th
932 Congreso Geológico Chileno v2: 102-106.
933 Cox, S, Knackstedt, M, Braun, J (2001) Principles of structural control on permeability and fluid flow in
934 hydrothermal systems. Society of Economic Geologist Reviews 14: 1-24.
935 Creixell, C, Arévalo, C (2009) Geología del Cuadrángulo El Tofo, Región de Coquimbo.
936 SERNAGEOMIN, Gobierno Regional de Coquimbo. mapa a escala 1:50.000. Santiago.
937 Creixell, C, Arévalo, C, Fanning, M (2009) Geochronology of the cretaceous magmatism from the
938 Coastal Cordillera of north-central Chile (29°15`to 29°30`S): metallogenic implications. XII Congreso
939 Geológico Chileno.
940 Doblas, M (1998) Slickenside kinematic indicators. Tectonophysics 295: 187-197.
941 Espinoza, S (1984) Le rôle du Crétacé inférieur dans la métallogénèse de la ceinture ferrifère d`Atacama-
942 Coquimbo, Chili. Doctoral thesis, l`Université Pierre et Marie Curie, Paris.
943 Espinoza, S (1990) The Atacama-Coquimbo ferriferous belt, northern Chile. In: Fontboté, L, Amstutz, G,
944 Cardozo, M, Cedillo, E, Frutos, J (eds) Stratabound ore deposits in the Andes. Berlin, Springer –
945 Verlag, pp 353–364.
946 Federico, L, Crispini, L Capponi, G (2010) Fault-slip analysis and transpressional tectonics: A study of
947 Paleozoic structures in northern Victoria Land, Antarctica. Journal of Structural Geology 32: 667-684.
948 Forsythe, R, Chisholm, L (1994) Paleomagnetic and structural constraints on the rotation in the northern
949 Chilean Coast Ranges. Journal of South American Earth Sciences 7: 279–295.
950 Geijer, P (1931) The iron ores of the Kiruna type. Sveriges Geologiska Undersökning C367, 39 p.
951 Gelcich, S, Davis, D, Spooner, T (2005) Testing the apatite-magnetite geochronometer: U-Pb and
952 40Ar/39Ar geochronology of plutonic rocks, massive magnetite-apatite tabular bodies, and IOCG
953 mineralization in Northern Chile. Geochimica and Cosmochimica Acta 69(13): 3367-3384.
954 Griffin, W, Powell, W, Pearson, N, O'Reilly, S (2008) GLITTER: data reduction software for laser
955 ablation ICP-MS. In: Sylvester, P. (ed), Laser Ablation–ICP–MS in the Earth Sciences. Mineralogical
956 Association of Canada Short Course Series Volume 40 (Appendix 2): 204-207.
957 Grocott J, Taylor G (2002) Magmatic arc fault system, deformation partitioning and emplacement of
958 granitic complexes in the Coastal Cordillera, north Chilean Andes (25°30'S to 27°00'S). Journal of
959 the Geological Society of London 159: 425–442.

960 Holdsworth, R, van Diggelen, E, Spiers, C, de Bresser, J, Walker, R, Bowen, L (2011) Fault rocks from
961 the SAFOD core samples: Implications for weakening at shallow depths along the San Andreas Fault,
962 California. Journal of Structural Geology 33: 132-144.
963 Ludwig, K. (2003) User's Manual for Isoplot 3.00 a Geochronological Toolkit for Microsoft Excel.
964 Marrett, R., Allmendinger, R.W. (1990) Kinematic analysis of fault-slip data. Journal of Structural
965 Geology 12: 973-986.
966 Marschik, R., Fontboté, L. (2001) The Candelaria-Punta del Cobre iron oxide Cu-Au (-Zn-Ag). Economic
967 Geology 96: 179-1826.
968 Marschik, R., Leveille, R.A., Martin, W. (2000) La Candelaria and the Punta del Cobre district, Chile:
969 Early Cretaceous iron oxide Cu-Au(-Zn-Ag) mineralization. In: Porter, T.M. (ed.): Hydrothermal iron-
970 oxide coppergold & related deposits: A global perspective: Adelaide, Australian Mineral Foundation,
971 pp 163–175.
972 Marschik, R., Singer, B.S., Munizaga, F., Tassinari, C., Moritz, R., Fontboté, L. (1997) Age of Cu (-Fe)-
973 Au mineralization and thermal evolution of the Punta del Cobre district, Chile. Mineralium Deposita
974 32: 531–546.
975 Mathur, R.D., Marschik, R., Ruiz, J., Munizaga, F., Martin, W. (2002) Age of mineralization of the
976 Candelaria iron oxide Cu-Au deposit, and the origin of the Chilean iron belt based on Re-Os isotopes.
977 Economic Geology 97: 59-71.
978 Ménard, J. (1986) Un modèle métasomatique pour les gisements de la Ceinture de fer du Chili. Académie
979 de Sciences [Paris] Comptes Rendus des Séances.II 302: 775-778.
980 Mpodozis, C., Ramos, V.A. (1990) The Andes of Chile and Argentina. In: Ericksen, G.E., Pinochet,
981 M.T.C., Reinemund, J.A. (eds.) Geology of the Andes and its relation to hydrocarbon and mineral
982 resources. Houston, Texas, Circum-Pacific Council for Energy and Mineral Resources, pp. 59–90.
983 Nyström, J.O., Henríquez, F. (1994) Magmatic features of iron ores of the Kiruna type in Chile and
984 Schweden: Ore textures and magnetite geochemistry. Economic Geology 89: 820–839.
985 Osterman, C. (1997) Mineralogical notes on the Productora project, Region III, Chile. Unpublished
986 report, General Minerals Corporation, May 1997, 8 pages.
987 Otsubo, M.; Yamaji, A. (2006) Improved resolution of the Multiple Inverse Method by eliminating
988 erroneous solutions. Computers and Geosciences 32: 1221-1227.

989 Oyarzún, .J, Frutos, .J. (1984) Tectonic and petrological frame of the Cretaceous iron deposits of north
990 Chile. Mining Geology 34: 21-31.
991 Park, C.F., Jr. (1972) The iron ore deposits of the Pacific basin. Economic Geology 67: 339-349.
992 Passchier, C.W., Trouw, R.A.J. (2005) Microtectonics. Berlin-Heilderberg, Springer-Verlag, 366 pp.
993 Pearce, N.J.G., Perkins, W.T., Westgate, J.A., Gorton, M.P., Jackson, S.E., Neal, C.R., Chenery, S.P.
994 (1997) A compilation of new and published major and trace element data for NIST SRM 610 and
995 NIST SRM 612 glass reference materials. Geostandard Newslett. 21: 115–144
996 .Petit, J. (1987) Criteria for the sense of movement on fault surfaces in the brittle rocks. Journal of
997 Structural Geology 9: 597–608.
998 Ray, G.E., Dick, L.A. (2002) The Productora prospect in North-Central Chile: An example of an intrusion
999 related, Candelaria Type Fe-Cu-Au Hydrotermal System. In: Porter, T.M. (Ed.) Hydrotermal Iron
1000 Oxide Copper-Gold & Related Deposits: A Global Perspective, Volume 2. PGC Publishing, Adelaide,
1001 Australia, pp. 131-151.
1002 Ritz, J. (1994) Determining the slip vector by graphical construction: use of a simplified representation of
1003 the stress tensor. Journal of Structural Geology 16(5): 737-741.
1004 Rojas, C., Beck, M., Burmester, R., Cembrano, J., Hervé, F. (1994) Paleomagnetism of the Mid-Tertiary
1005 Ayacara Formation, southern Chile: counterclockwise rotation in a dextral shear zone. Journal of
1006 South American Earth Sciences 7: 45–56.
1007 Roperch, P., Sempere, T., Macedo, O., Arriagada, C., Fornari, M., Tapia, C., Garcia, M., Laj, C. (2006)
1008 Counterclockwise rotation of late Eocene-Oligocene fore-arc deposits in southern Peru and its
1009 significance for oroclinal bending in the central Andes. Tectonics 25: TC3010.
1010 Ruiz, C., Peebles, F. (1988) Geología, distribución y génesis de los yacimientos metalíferos chilenos.
1011 Santiago, Editorial Universitaria, 334 pp.
1012 Ruiz, C., Aguirre, L., Corvalan, J., Klohn, C., Klohn, E., Levi, B. (1965) Geología y yacimientos
1013 metalíferos de Chile: Instituto de Investigaciones Geológicas [Chile], 386 p.
1014 Selby, D., Creaser, R. (2001) Re-Os Geochronology and systematics in molybdenite from the Endako
1015 Porphyry Molybdenum Deposit, British Columbia, Canada. Economic Geology 96:197-204.
1016 Scheuber, E., González, G. (1999) Tectonics of the Jurassic-Early Cretaceous arc of the north Chilean
1017 Coastal Cordillera (22°-26°S): A story of crustal deformation along a convergent plate boundary.
1018 Tectonics 18: 895-910.

1019 Scheuber, E., Andriessen, P. (1990) The kinematic and geodynamic significance of the Atacama Fault
1020 Zone, northern Chile. Journal of Structural Geology 12: 243-250.
1021 Scholz, C. (2002) The Mechanics of Earthquakes and Faulting. Cambridge Press, second edition,
1022 Cambridge, UK, 470pp.
1023 Sibson, R.H. (1987) Earthquake rupturing as a mineralizing agent in hydrothermal systems. Geology 15:
1024 701-704.
1025 Sillitoe R. H. (2003) Iron oxide-copper gold deposits: an Andean review. Mineralium Deposita 38: 787-
1026 812.
1027 Sippel, J., Scheck-Wenderoth, M., Reicherter, K., Mazur, S. (2009) Paleostress states at the south-western
1028 margin of the Central European Basin System – Application of fault slip analysis to unravel polyphase
1029 deformation pattern. Tectonophysics 470: 129-146.
1030 Sperner, B., Zweigel, P. (2010) A plea for more caution in fault-slip analysis. Tectonophysics 482: 29-41.
1031 Tauxe, L. (1998) Paleomagnetic Principles and Practice. Modern Approaches in Geophysics. Kluwer
1032 Academic, Amsterdam.
1033 Taylor, G., Grocott, J., Pope, A., Randall, D. (1998) Mesozoic faults systems, deformation and fault block
1034 rotation in the Andean forearc: a crustal-scale strike-slip duplex of the Coastal Cordillera of northern
1035 Chile. Tectonophysics 299: 93-109.
1036 Taylor, G., Grocott, J., Dashwood, B., Gipson, M., Arevalo, C. (2007) Implications for crustal rotation
1037 and tectonic evolution in the central Andes fore arc: New paleomagnetic results from the Copiapo
1038 region of northern Chile, 26º-28ºS: Journal of Geophysical Research-Solid Earth 112: B01102.
1039 Thomson, S.N., Gehrels, G.E., Ruiz, J., Buchwaldt, R. (2012) Routine low-damage U-Pb dating of apatite
1040 using laser ablation-multicollector-ICPMS. Geochemistry, Geophysics, Geosystems 13: Q0AA21,
1041 doi:10.1029/2011GC003928.
1042 Ullrich, T. D., Clark, A. H. (1999) The Candelaria copper-gold deposit, Region III, Chile: Paragenesis,
1043 geochronology and fluid composition. In: Stanley, C.J. et al. (eds.) Mineral Deposits: Processes to
1044 Processing. Rotterdam, Balkema, pp. 201–204.
1045 Veloso, E., Anma, R., Yamaji, A. (2009) Heterogeneous Paleostress Regimes Recorded on the Taitao
1046 Ophiolite (Southern Chile), Implications for Ophiolite Emplacement and Effects of the Subduction of
1047 the Chile Ridge System. Andean Geology 36(1): 3-16.

1048 Vila, T., Lindsay, N., Zamora, R. (1996) Geology of the Manto Verde copper deposit, northern Chile: A
1049 specularite-rich, hydrothermal-tectonic breccia related to the Atacama fault zone. Society of
1050 Economic Geology Special Publication 5: 157–170.
1051 Vivallo, W., Díaz, A., Jorquera, R. (2008) Yacimientos metalíferos de la región de Atacama, Escala
1052 1:500.000. Carta Geológica de Chile, Serie Recursos Minerales y Energéticos (n.27).
1053 SERNAGEOMIN, Santiago, 72 pp.
1054 Vivallo, W. Hemnriquez, F., Espinoza, S. (1995) Metasomatismo y alteración hidrotermal en el distrito
1055 ferrífero Cerro Negro Norte, Copiapó, Chile. Revista Geológica de Chile 22: 75-88.
1056 Vivallo, W. (2009) Yacimientos de óxidos de Hierro-Cobre-Oro en Chile. XII Congreso Geológico
1057 Chileno: s11_060.
1058 Wallace, R. (1951) Geometry of shearing stress and relation to faulting, Journal of Geology 59: 118-130.
1059 Whitney, D., Evans, B. (2010) Abbreviations for names of rock-forming minerals. American Mineralogist
1060 95: 185-187.
1061 Woodcock, N.H., Mort, K. (2008) Classification of fault breccias and related fault rocks. Geological
1062 Magazine 145(3): 435–440.
1063 Yamaji, A. (2000) The Multiple Inverse Method: A new technique to separate stresses from
1064 heterogeneous fault-slip data. Journal of Structural Geology 22: 441-452.
1065 Žalohar, J., Vrabec, M. (2007) Paleostress analysis of heterogeneous fault-slip data: The Gauss method.
1066 Journal of Structural Geology 29: 1798-1810.
1067 Žalohar, J., Vrabec, M. (2008) Combined kinematical and paleostress analysis of fault-slip data: The
1068 multiple-slip method. Journal of Structural Geology.30: 1603-1613.
1069
1070 Figure Captions
1071
1072 Figure 1. General location of Fe-rich deposits in northern Chile showing the general trace of the AFS
1073 (after Cembrano et al., 2005) and of the “Cretaceous Iron Belt” (e.g. Sillitoe, 2003).
1074 Figure 2. (a) Contour density (each 2%) plot of poles of all measured structural elements at Dominga and
1075 indicating preferential orientations (A to E). Rose diagrams (petals each 5º) showing: (b) same
1076 data as (a) as well as identified preferential strike directions; (c) the strike orientation of
1077 structural elements with complete fault datum (fault-slip data); (d) the strike orientation of

1078 ultracataclasites and cataclasites with S-C textures. (e) Half-rose diagram (5º petals) showing
1079 the preferential strike direction of veins with different mineral fillings.
1080 Figure 3. Examples of the variety of structural elements outcropping at Dominga: (a) foliated, right-lateral
1081 ultracataclasite with S-C texture; (b) ultracataclasite with large Mag crystals; (c) contiguous set
1082 of structural elements (cataclasites, fault-breccias) forming the composite structural element of
1083 El Tofo Deformation Band; (d) hydrothermal breccia with Mag>Act(>>Ap?) matrix, including
1084 large Fe-altered clast of the Punta del Cobre Formation; (e) hydrothermal breccia with Mag-
1085 rich matrix and large clast of the Porphyric Dioritic Complex (andesite); (f) slickenlines on a
1086 slip-surface developed on the Porphyric Dioritic Complex; (g) slickenfibers of Hem (specular)
1087 on an air-exposed fault-vein; (h) quartz veins with two different textures showing cutting
1088 relationship; (i) subvertical, centimeter-wide, Mag-rich veins cutting the Punta del Cobre
1089 strata; (j) histogram of occurrence and (k) box-and-whisker plot of thicknesses of the different
1090 structural elements filtered by preferential striking direction.
1091 Figure 4. Examples of mapped key locations at the Dominga district. (a) Satellite view (Google Earth®)
1092 showing the Dominga district (datum UTM19S, WGS82). (b) to (e) inlets show mapped
1093 lineaments and structural elements.
1094 Figure 5. Lower hemisphere, equal-area projections of density contours of P (left) and T (right) strain
1095 axes from (a) entire fault-slip data and from the filtered fault-slip data: (b) ESS, (c) S-C-
1096 derived fault-slip data, (d) ETSS, (e) ISS, and (f) LSS.
1097 Figure 6. Lower hemisphere, equal-area projections with solutions of principal stress axes estimated with
1098 the MIM from (a) the entire (unfiltered) fault-slip data, and (b) the S-C-derived (identified
1099 clusters are labeled A to F, an indicated on both the stereogram and the distribution of ϕ). (c)
1100 histogram of misfit angles between measured fault-slip data and estimated stress field
1101 (indicated). (d) sets of structural elements activated under each of the different estimated stress
1102 fields (A-F) showing their compatible displacement direction and the estimated direction of
1103 principal stress axes color coded according to its ϕ value.
1104 Figure 7. Relative chronology among and between key minerals observed at Dominga together with
1105 defined alteration/mineralization stages (I-IV) (width of triangles indicates relative abundance).
1106 (b) to (k) micro-photographs with examples of the occurrences and relationships of key

minerals: (b) pervasive Mag-Bt alteration (stage I) of strata from Punta del Cobre Formation; (c) coarse-grained Mag-Act association (stage IIa); (d) Magnetite porphyroblast with Qtz syntectonic rims (stage IIa) in a fine-grained Mag-rich matrix (stage I); (e) matrix of hydrothermal breccia from the ESS with Mag-Act-Ap-Qtz (stage IIb) association; (f) occurrence of Ab-Ep-Qtz association (stage IIIa) in rocks of the Porphyric Dioritic Complex; (g) intergrowth of Aln and Ccp together with Anh (stage IIIb); (h) veins with infill of Qtz and Ep (stages III-IV) association; (i) anhedral Vrm crystals (stage IIIb) cut by vein of Cal (stage IV); (j) partial view of a Cal-rich vein with lattice and banded textures, together with tiny crystals of Ccp (stage IV); (k) partial view of a vein with Hem and Qtz association filling (stage IV). Microphoto (b) taken under transmitted polarized light and (j) under reflected polarized light, all others under transmitted cross-polarized light.

Figure 8. Conceptual sketch profile view of a (strike-slip) structural element and its relation to different structural levels (after Sibson, 1987; Scholz, 2002; Holdsworth et al., 2011).

Figure 9. Samples and data used for isotopic dating. (a) Photo (upper) and SEM image (lower) of mineral association seen on sample DS11-134 (see Table 1) used for Re-Os isotopic dating. (b) Same as (a) but showing sample DN11-136 used for U-Pb isotopic dating, (c) Concordia U-Pb plot with calculated age for the apatite (data-point error ellipses are 68.3%).

Figure 10. General estimated directions of principal (a) strain and (b) stress axes for the entire fault-slip data (top) and for each of the identified structural systems (senses and amounts of rotation/shift of principal axes from one system to the other are indicated). (c) Relative time-trajectory of the estimated maximum principal strain and stress axes for each structural system. Sense and amount of rotation/shift plus the main tectonic setting, TP (transpressive) or TT (transtensive) are indicated.

Figure 11. Compilation of geochronological ages of regional and local tectonic, magmatic, structural and of alteration/mineralization stages identified and defined at Dominga and at other Fe-rich deposits in the "Cretaceous Iron Belt". TT: Transtensional, TP: Transpressional

Figure 12. Schematic cartoon showing the tectono-metallogenic relation and evolution between and among the different structural systems and defined alteration/mineralization stages (I to IV).

Figure 1
Click here to download Figure: Veloso et al. - Figure 1.tif

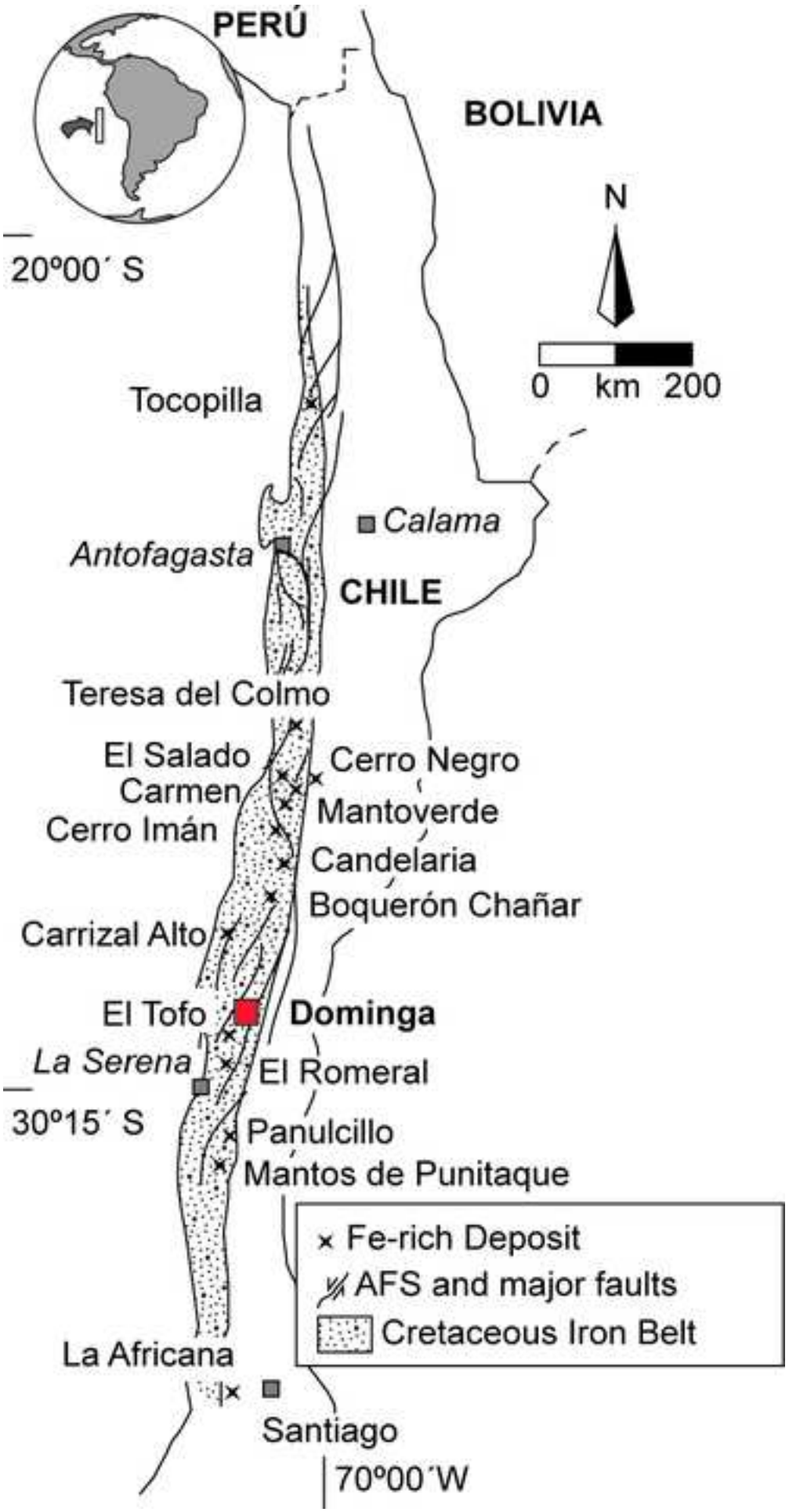

Figure 2
Click here to download Figure: Veloso et al. - Figure 2.tif

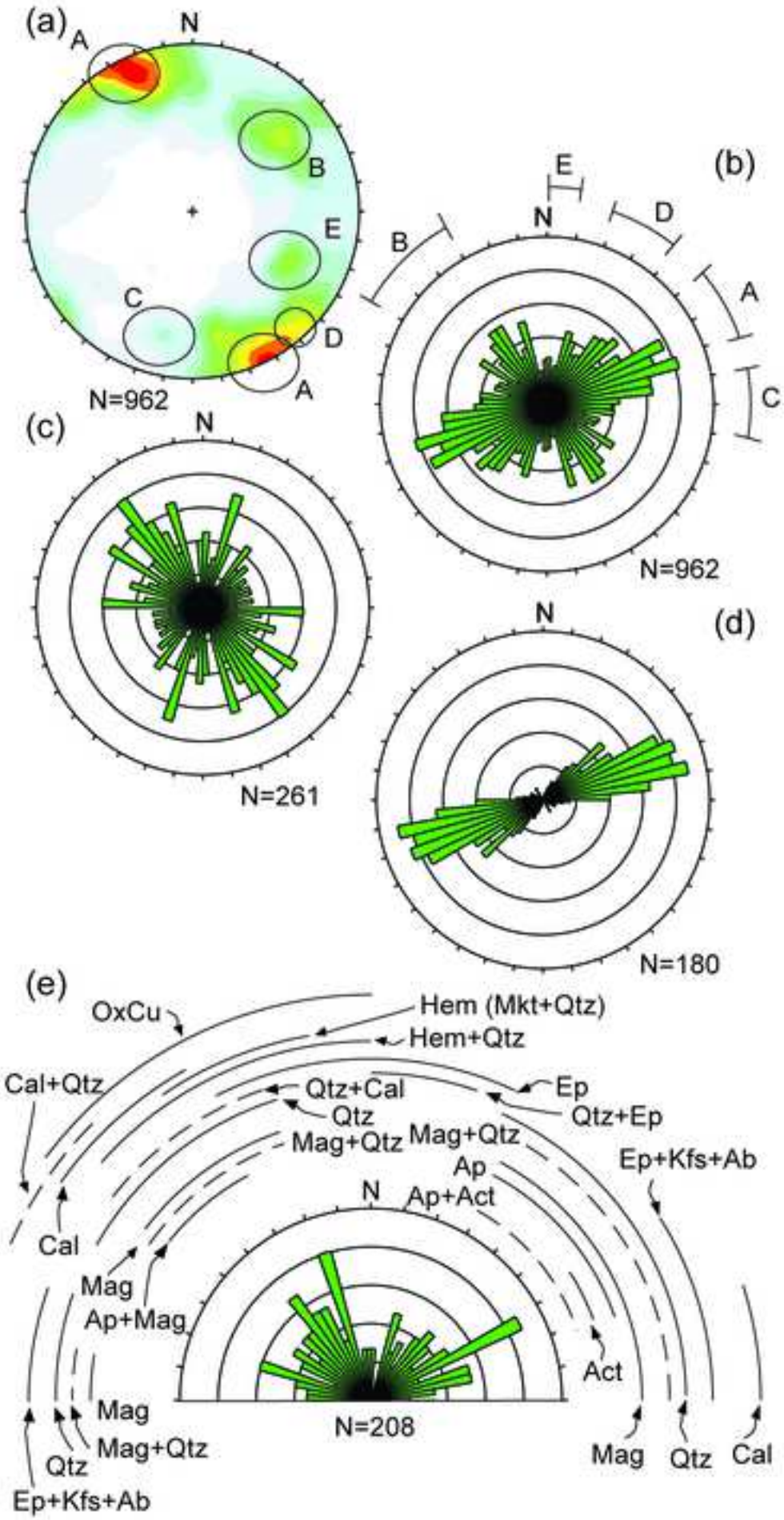

Figure 3
Click here to download Figure: Veloso et al. - Figure 3.tif

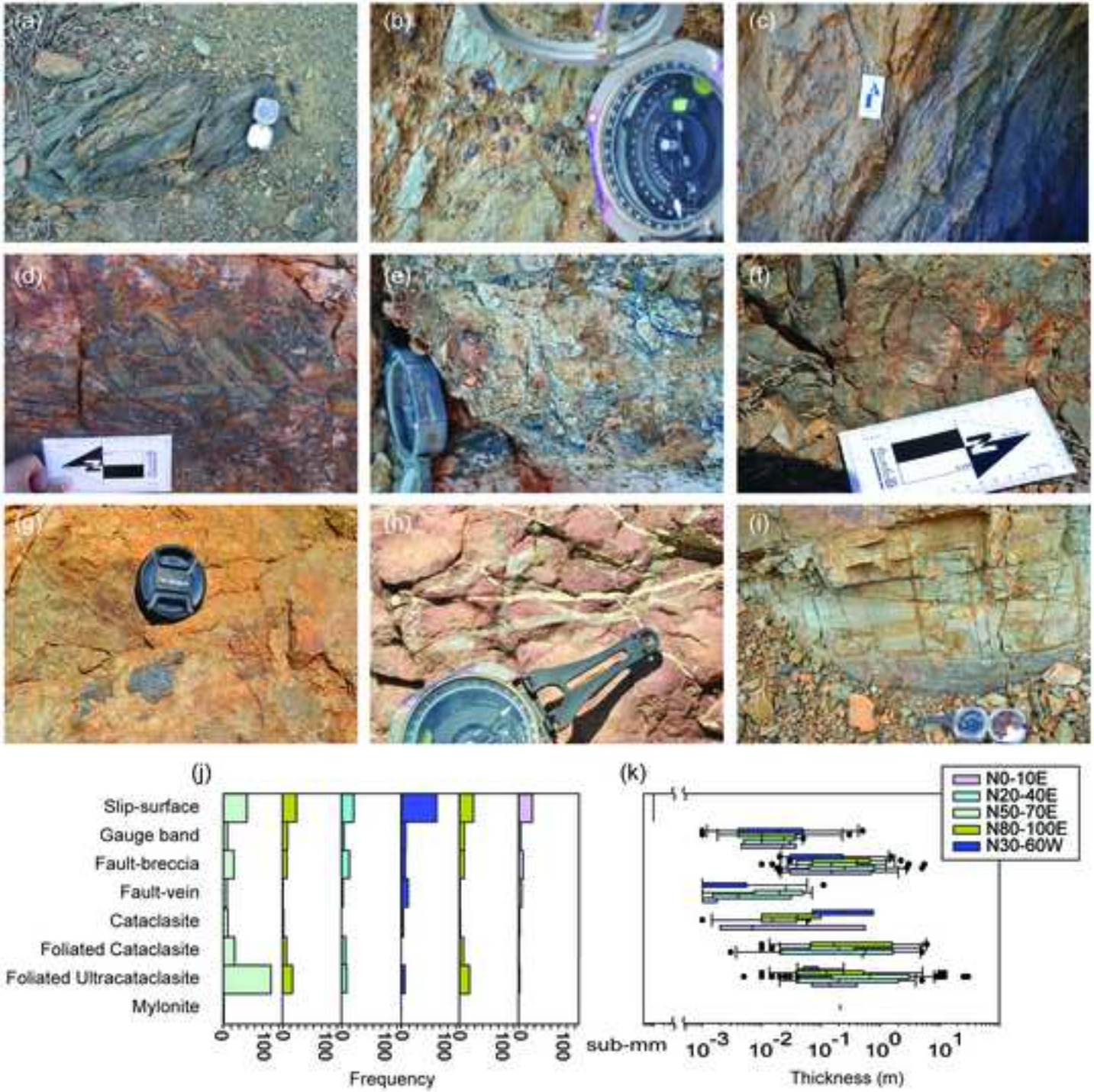

Figure 4
Click here to download Figure: Veloso et al. - Figure 4.tif

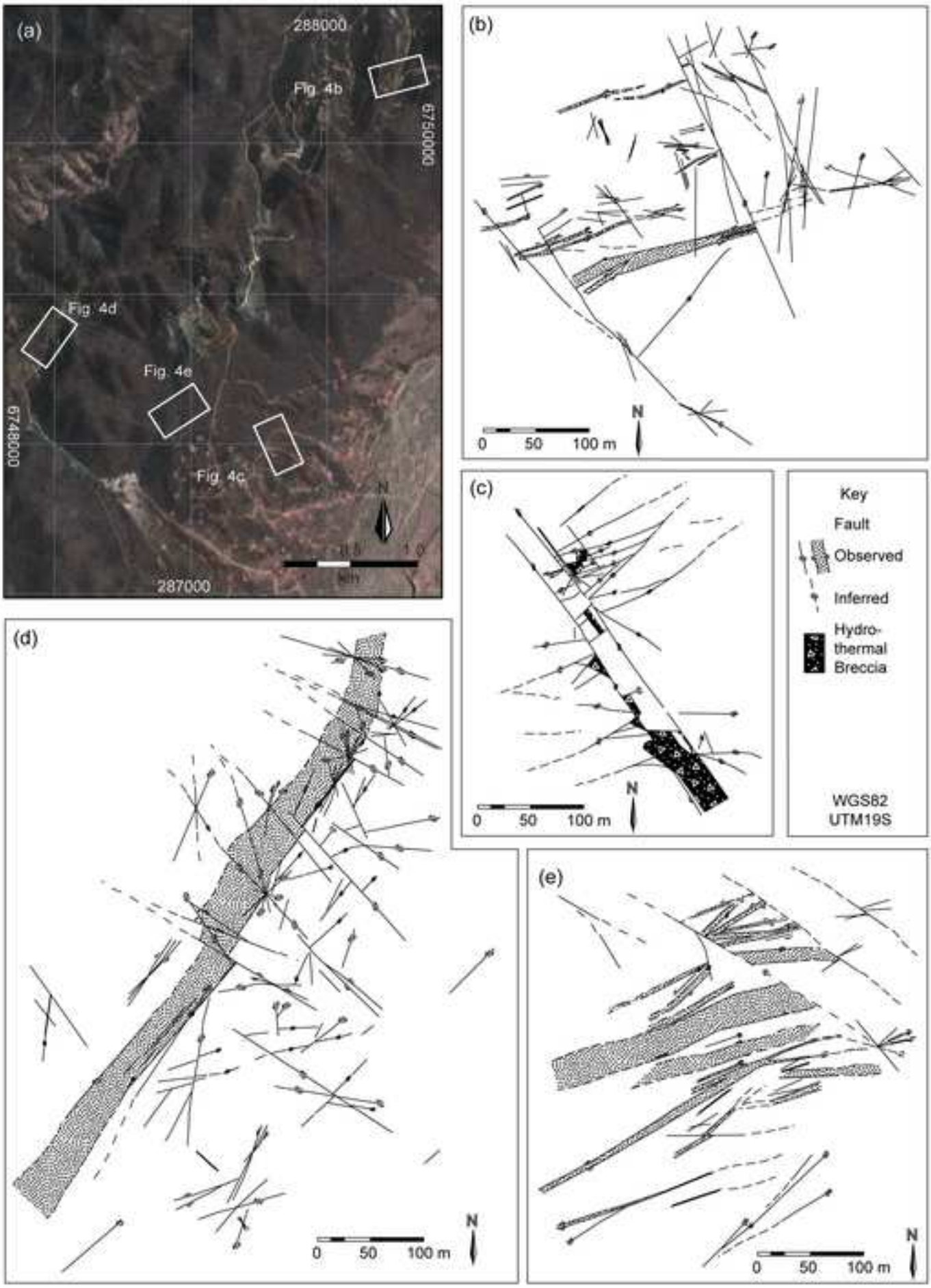

Figure 5
Click here to download Figure: Veloso et al. - Figure 5.tif

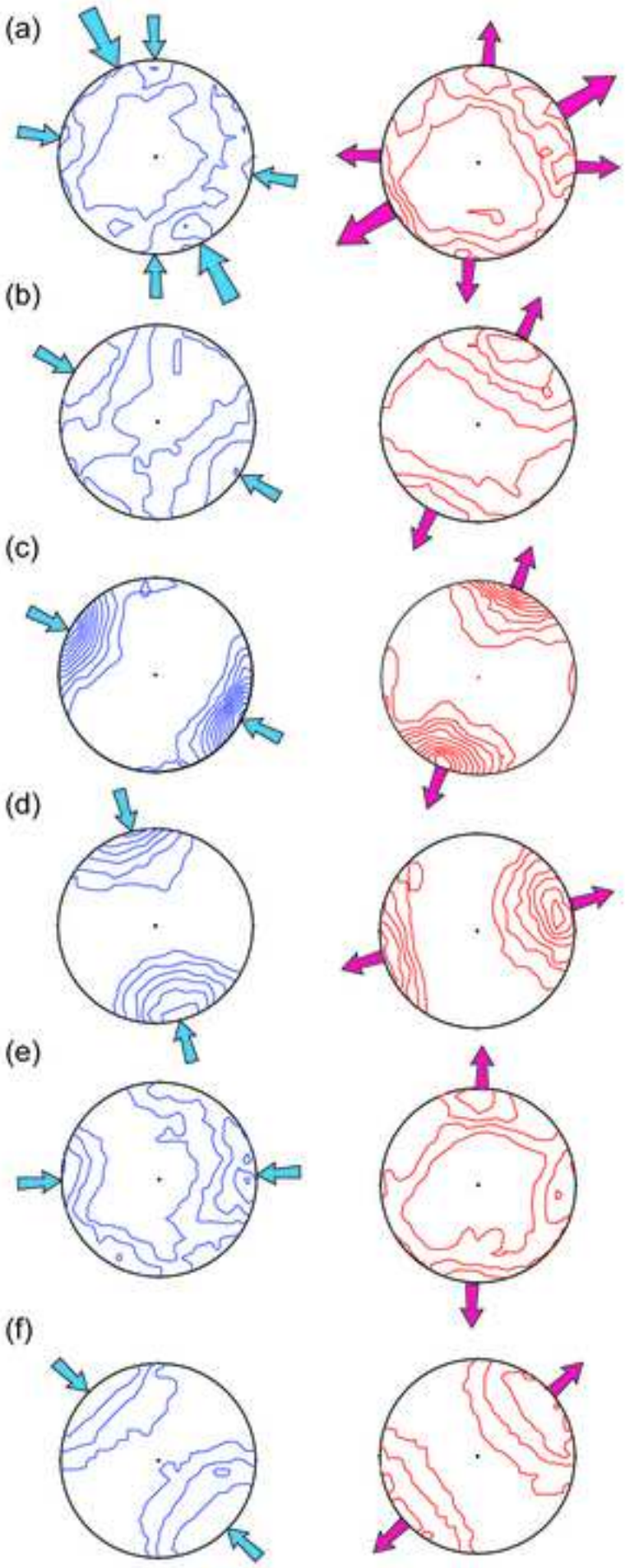

Figure 6
Click here to download Figure: Veloso et al. - Figure 6.tif

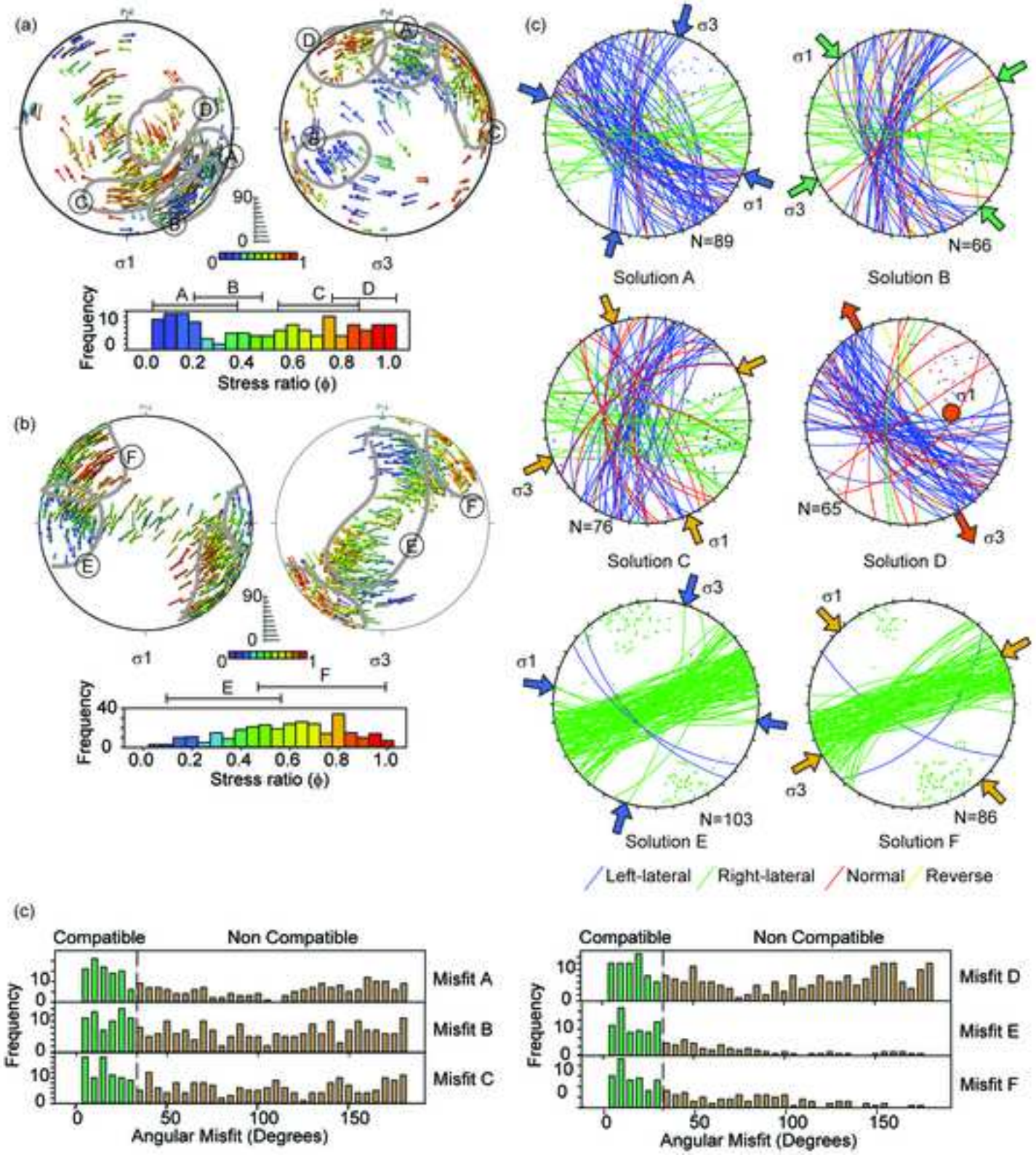

Figure 7

Click here to download Figure: Veloso et al. - Figure 7.tif

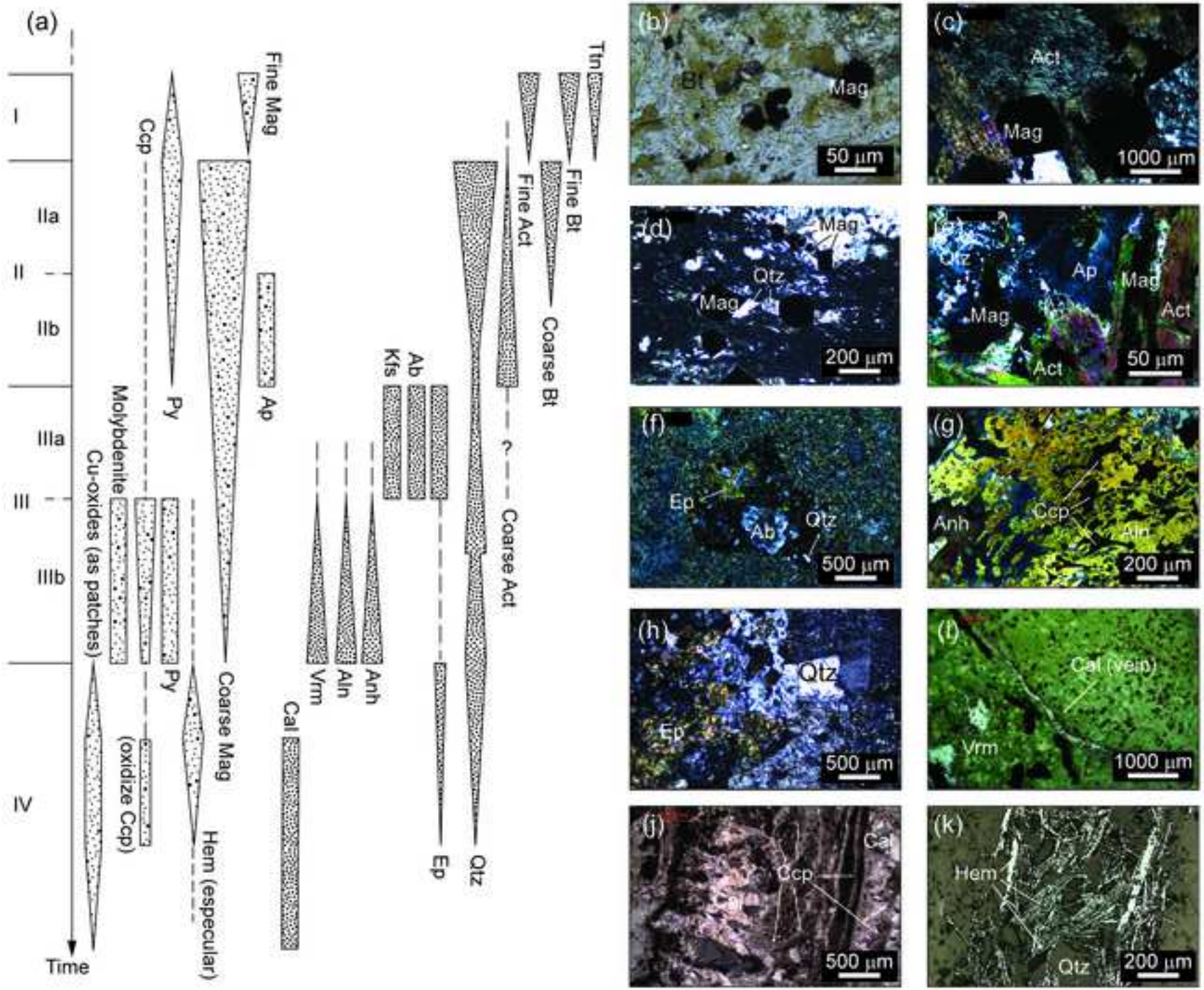

Figure 8
Click here to download Figure: Veloso et al. - Figure 8.tif

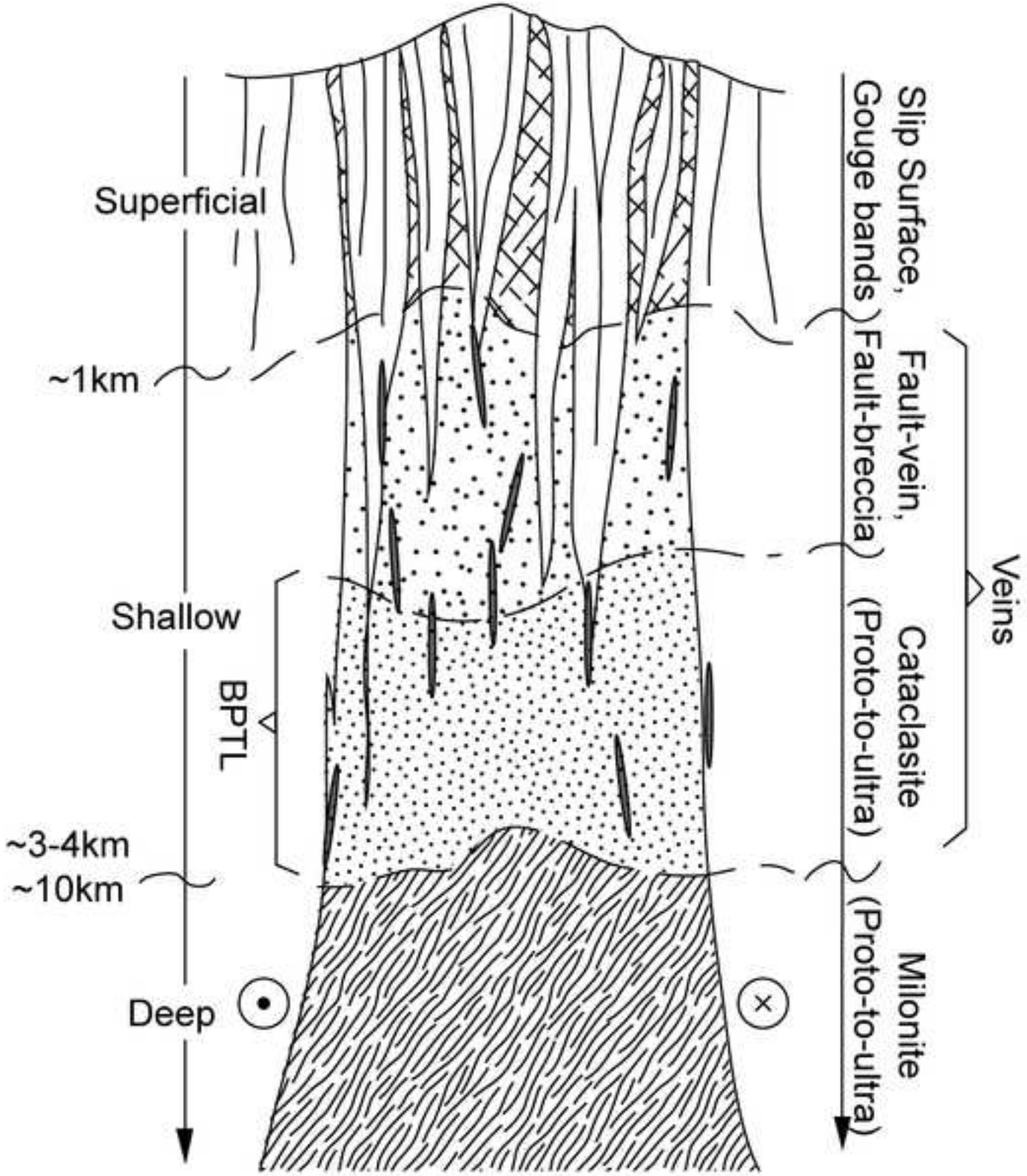

Figure 9
Click here to download Figure: Veloso et al. - Figure 9.tif

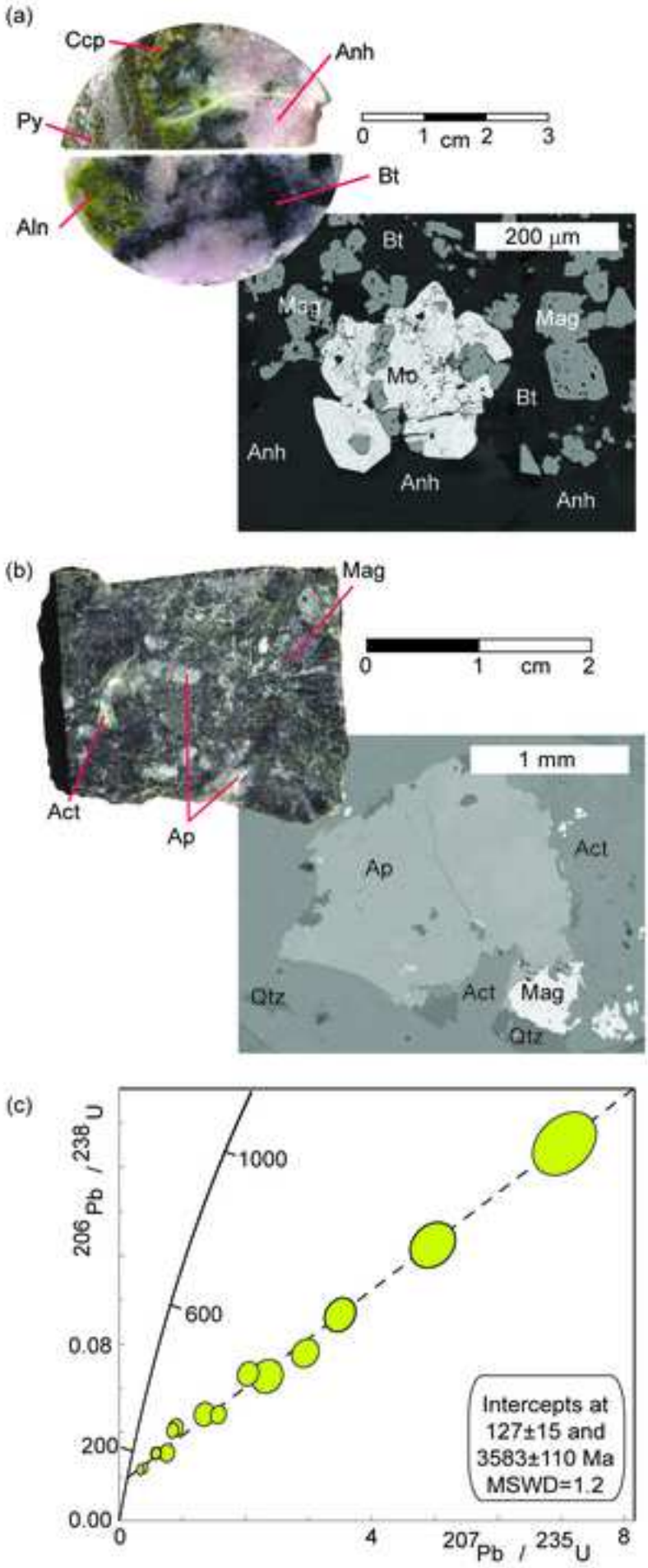

Figure 10
Click here to download Figure: Veloso et al. - Figure 10.tif

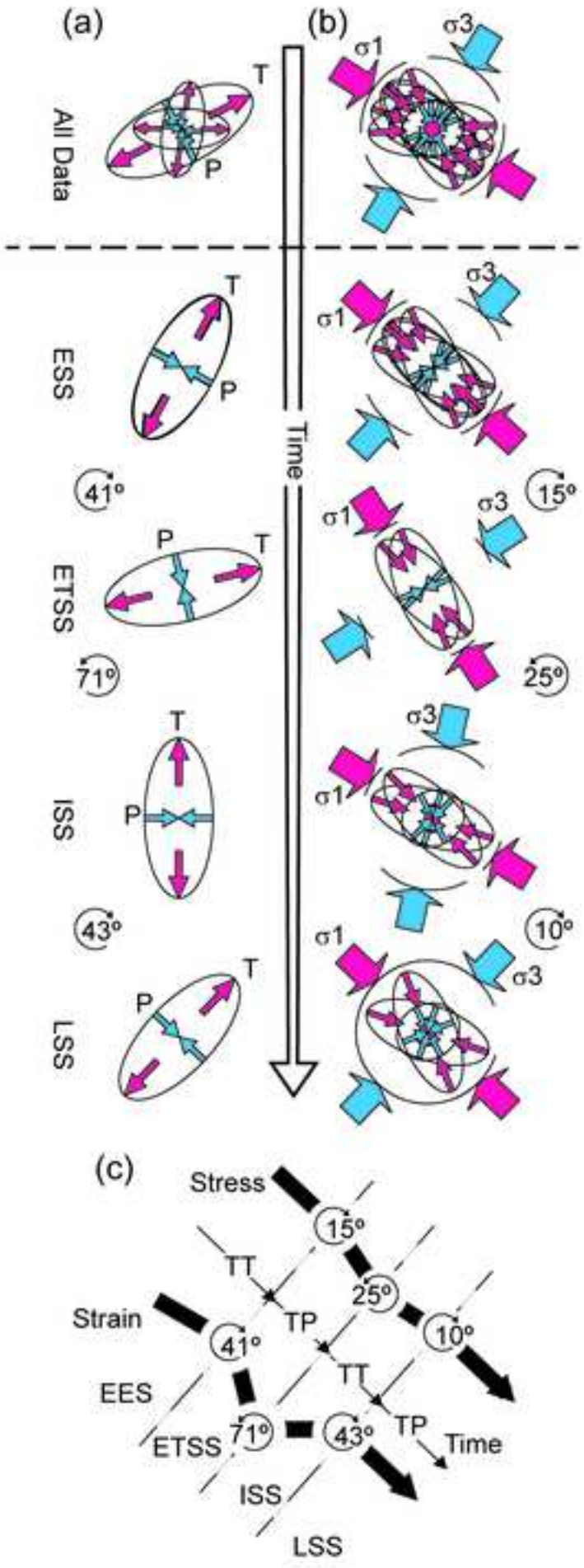

Figure 11

Click here to download Figure: Veloso et al. - Figure 11.tif

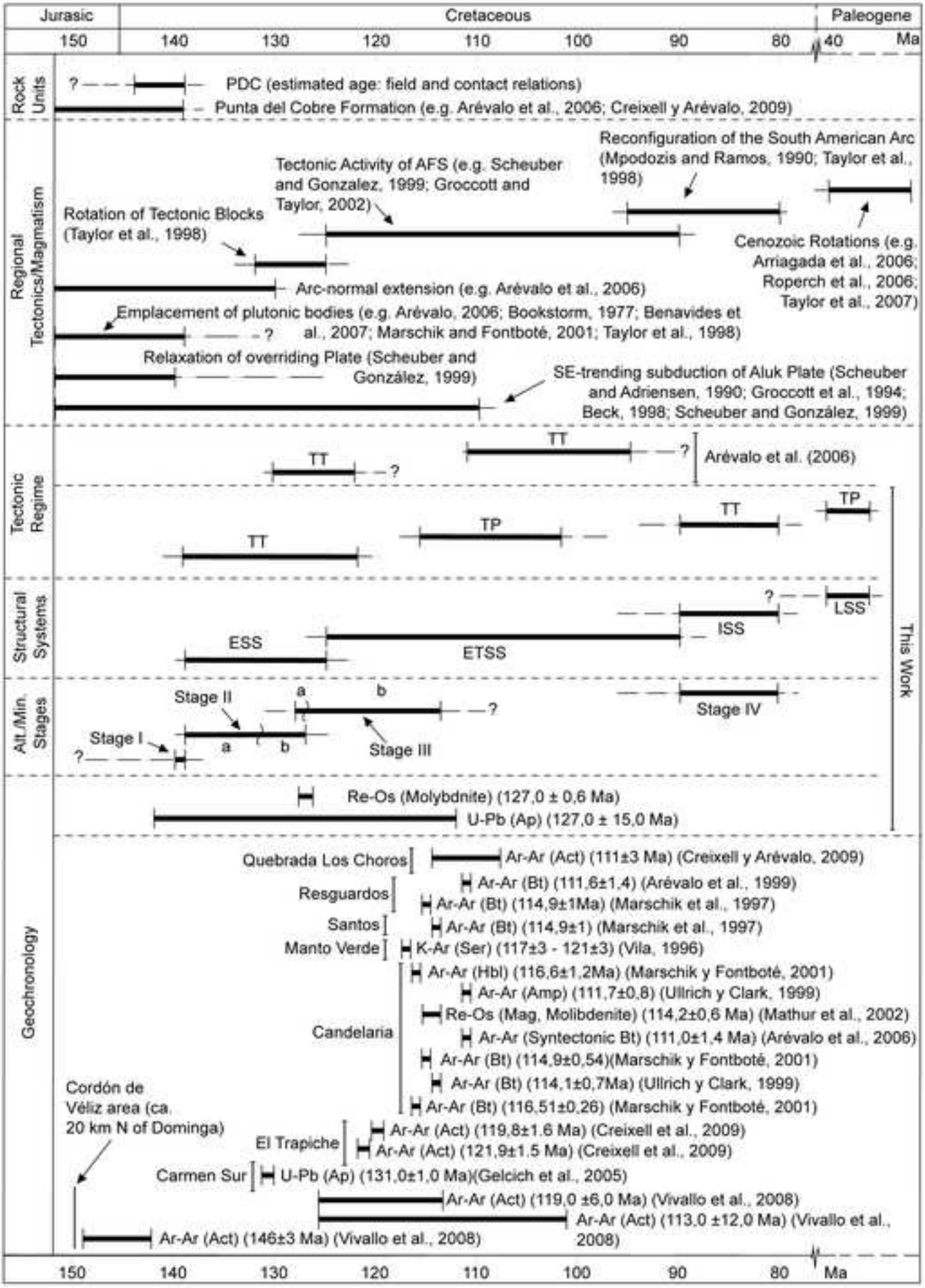

Figure 12

Click here to download Figure: Veloso et al. - Figure 12.tif

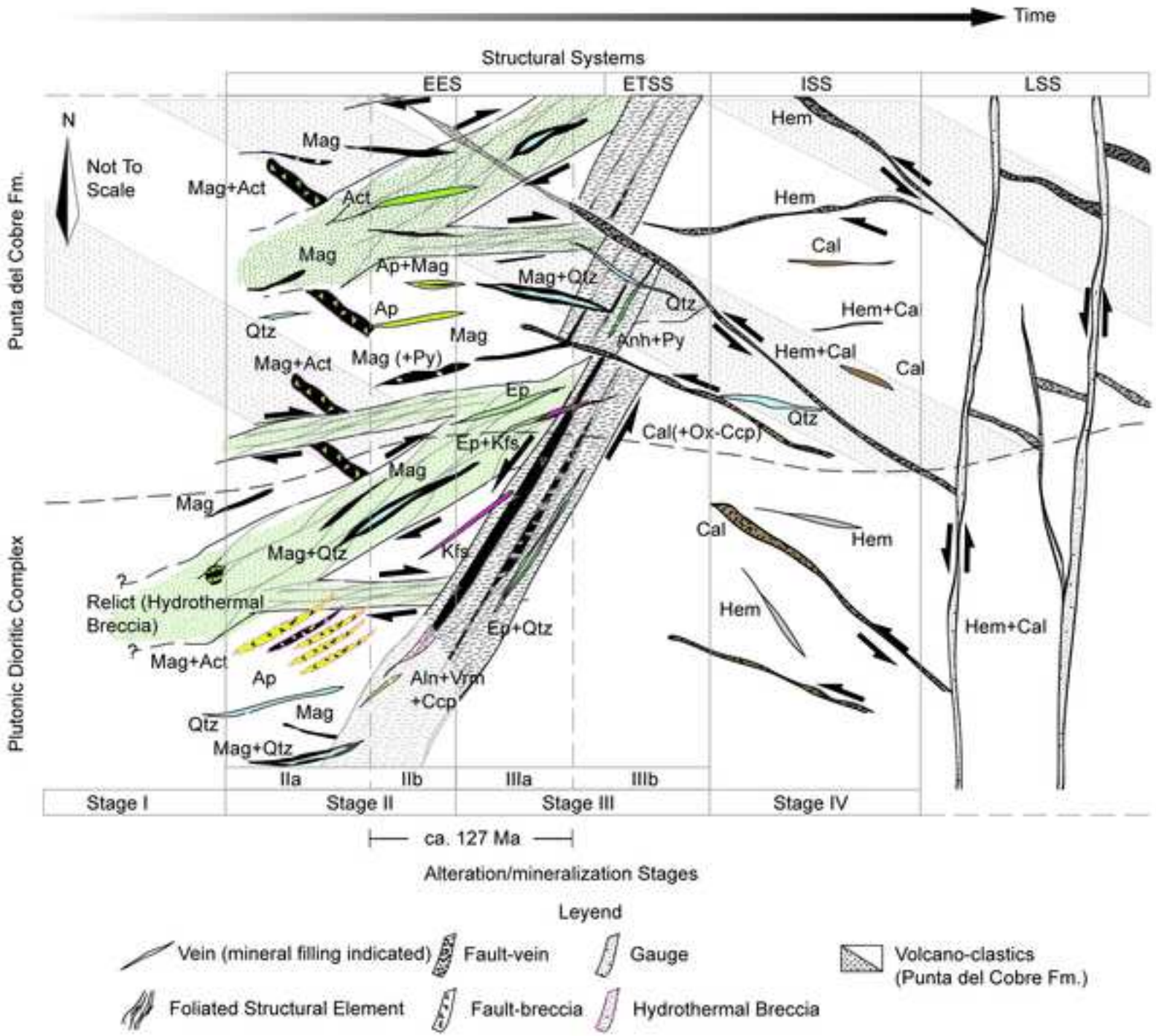

Table 1

Structural Systems and Paragenetic Assemblages at the Dominga Fe-Cu Deposit: Tectono-Metallogenic Evolution

Veloso, E.[1] (corresponding author), Email: eaveloso@gmail.com

Cembrano, J.[2], Email: jcembrano@ing.puc.cl

Arancibia, G.[2], Email: garancibia@ing.puc.cl

Heuser, G.[2], Email: gkheuser@uc.cl

Neira, S.[3], Email: sergio.neira@andesiron.cl

Siña, A.[3], Email: armando.sina@andesiron.cl

Garrido, I.[3], Email: ivan.garrido@andesiron.cl

Vermeesch, P.[4], Email: p.vermeesch@ucl.ac.uk

Selby, D. [5], Email: david.selby@durham.ac.uk

Santibáñez, I.[2], Email: ivsantibanez@uc.cl

Pérez-Flores, P.[2], Email: pvperez1@uc.cl

Gomila, R.[2], Email: ragomila@uc.cl

[1] Fundación Norte Sustentable, Avenida Cerro El Plomo 5460, Piso 19, Las Condes, Santiago, Chile.

[2] Departamento de Ingeniería Estructural y Geotécnica, Pontificia Universidad Católica de Chile, Avenida Vicuña Mackenna 4860, Macul, Santiago, Chile.

[3] Andes Iron SpA, Avenida Cerro El Plomo 5460, Piso 19, Las Condes, Santiago, Chile.

[4] Department of Earth Sciences, University College London, Gower Street, London WC1E 6BT, UK.

[5] Department of Earth Sciences, University of Durham, Durham DH1 3LE, UK.

26

27 Table 1. Geochronologic isotopic data.

28

Re-Os data for molybdenite

Sample	Weight (mg)	Re (ppm)	± 2□	^{187}Re (ppm)	± 2□	^{187}Os (ppb)	± 2□	Age (Ma)	± 2□
DS11-134	0.005	886.46	8.03	557.16	5.05	1180.92	10.45	127.09	0.65

U/Pb data for apatite

Sample	Concentration (ppm)			Ratio					
	U	Th	Th/U	^{207}Pb/^{206}Pb	1σ	^{207}Pb/^{235}U	1 σ	^{206}Pb/^{238}U	1 σ
DG11-136-G1-01	0.28	1.39	5.06	0.260	0.026	2.344	0.164	0.065	0.005
DG11-136-G1-02	0.41	1.01	2.49	0.272	0.018	3.499	0.162	0.093	0.005
DG11-136-G1-03	0.51	1.10	2.14	0.222	0.016	2.043	0.110	0.67	0.004
DG11-136-G1-04	0.51	1.13	2.23	0.203	0.021	1.350	0.106	0.048	0.004
DG11-136-G1-05	.42	1.42	3.38	0.155	0.016	0.900	0.075	0.042	0.003
DG11-136-G2-01	1.29	0.38	0.30	0.121	0.013	0.400	0.036	0.024	0.002
DG11-136-G2-02	0.84	0.83	1.00	0.151	0.013	0.850	0.059	0.041	0.002

DG11-136-G2-03	0.54	0.97	1.78	0.179	0.024	0.758	0.077	0.031	0.003
DG11-136-G2-04	0.58	0.79	1.36	0.139	0.015	0.584	0.052	0.031	0.002
DG11-136-G2-05	1.18	0.57	0.48	0.106	0.013	0.339	0.036	0.023	0.002
DG11-136-G3-01	0.37	1.44	3.93	0.281	0.020	2.950	0.143	0.076	0.004
DG11-136-G3-03	0.25	1.15	4.62	0.288	0.020	4.966	0.236	0.125	0.007
DG11-136-G3-04	0.24	0.39	1.58	0.299	0.020	7.051	0.332	0.171	0.009
DG11-136-G3-05	1.19	16.02	13.42	0.237	0.018	1.572	0.081	0.048	0.003

29

30